Journal of Luminescence 289 (2026) 121670

Contents lists available at ScienceDirect

Journal of Luminescence

journal homepage: www.elsevier.com/locate/jlumin

Full Length Article

Structural modulation and Judd–Ofelt-guided luminescence enhancement in Eu^{3+}-doped $LiCa_4O(BO_3)_3$ via dual-alkali co-doping

Jabir Hakami [a], M.B. Coban [b], H. Aydin [c,d], U.H. Kaynar [e], M. Sharahili [a], O. Madkhali [a], D. Somaily [a], N. Can [a,*]

[a] Jazan University, College of Science, Department of Physical Sciences, Physics Division, P.O. Box 114, 45142, Jazan, Saudi Arabia
[b] Balikesir University, Faculty of Arts and Sciences, Department of Physics, Balikesir, Turkiye
[c] Graphene Application&Research Center, Izmir Katip Celebi University, Izmir, Turkiye
[d] Central Research Laboratories, Izmir Katip Celebi University, Izmir, Turkiye
[e] Bakırcay University, Faculty of Engineering and Architecture, Department of Fundamental Sciences, Menemen, Izmir, Turkiye

ARTICLE INFO

Keywords:
$LiCa_4O(BO_3)_3$
Eu^{3+} doping
Alkali co-doping
Photoluminescence
Judd–Ofelt analysis
Thermal stability
Red phosphors

ABSTRACT

Eu^{3+}-doped borates stand out as promising red-emitting phosphors owing to their stable crystal structures and sharp luminescence features. In this study, we investigate $LiCa_4O(BO_3)_3$:Eu^{3+} and explore how additional doping with K^+ and Na^+ ions influences the symmetry of Eu^{3+} sites, photoluminescence efficiency, and thermal stability. All synthesized samples exhibit a single-phase orthorhombic structure. Photoluminescence spectra revealed prominent Eu^{3+} emissions, dominated by the $^5D_0 \rightarrow {}^7F_2$ transition at 613 nm. Remarkably, co-doping with alkali metals enhances the long-wavelength emission (~705 nm), contributing to deeper red color output. Judd–Ofelt analysis showed that Na^+-doped and Eu-only samples maintained Ω_4-dominant profiles, indicating a relatively symmetric local environment. In contrast, K^+ doping significantly increased the Ω_2/Ω_4 ratio, suggesting a more asymmetric crystal field and stronger electric-dipole transitions. Lifetime and non-radiative decay measurements supported these findings, showing that K^+ improved radiative efficiency, while Na^+ preserved structural rigidity with moderate trade-offs in emission strength. Thermal quenching studies revealed activation energies of ~0.36 eV for Eu-only samples, decreasing to ~0.15 eV with alkali co-doping, confirming enhanced thermal stability. Chromaticity data indicated tunable red emission, where K^+ contributed to higher color purity and Na^+ offered better thermal color retention. These insights underline how alkali ions fine-tune site symmetry and emission behavior, providing useful guidance for designing advanced Eu^{3+}-based borate phosphors for LED and optical sensing applications.

1. Introduction

Rare-earth doped inorganic phosphors continue to attract substantial interest due to their excellent thermal and chemical stability, sharp emission lines, and suitability for a wide range of photonic applications, including white light-emitting diodes (WLEDs), display technologies, and dosimetry. Among various host matrices, lithium calcium borate has been extensively studied owing to its wide band gap, low phonon energy, and favorable coordination sites for rare-earth ions [1–3]. Its orthorhombic structure (space group *Pbca*) offers a stable and optically transparent lattice that accommodates activator ions with minimal lattice strain.

Several borate hosts, including $YBa_3(BO_3)_3$, $Sr_3(BO_3)_2$, and $Li_2B_4O_7$, have been studied for rare-earth doping due to their structural tunability and stability [4–6]. $LiCaBO_3$ is well studied due to its simple structure, low synthesis temperature, and ability to host activator ions such as Eu^{3+}, Tb^{3+}, Sm^{3+}, and Dy^{3+} [2,7,8]. Despite similar abbreviations, $LiCa_4O(BO_3)_3$ (LiCBO) and $LiCaBO_3$ (LCB) are distinct compounds with different chemical compositions and crystal structures. Despite the extensive studies on LCB, the more structurally complex compound LiCBO remains largely unexplored. The higher Ca^{2+} content and flexible coordination sites of LiCBO provide an opportunity for improved rare-earth incorporation and tunable luminescence. Recent studies indicate that alkali co-doping not only compensates charge but also enhances luminescence and alters Eu^{3+} site symmetry [4,9,10].

Recent reviews have emphasized the importance of host lattice

* Corresponding author.
E-mail address: ncan@jazanu.edu.sa (N. Can).

https://doi.org/10.1016/j.jlumin.2025.121670
Received 3 October 2025; Received in revised form 3 November 2025; Accepted 17 November 2025
Available online 20 November 2025

design and alkali co-doping for optimizing emission intensity and thermal stability [11]. Although single alkali dopants have been investigated, the synergistic effects of Na^+ and K^+ co-doping in borate hosts remain unexplored. Insights from silicate and phosphate systems suggest that mixed-alkali substitution, which depend strongly on the relative size and field strength of the alkali ions, can tune site symmetry and electron–phonon interactions, thus motivating a systematic study in LiCBO [9,12,13].

The host structure investigated in this study, LiCBO represents a structurally richer analogue of LCB. It contains a higher concentration of Ca^{2+} ions and interstitial O^{2-}, which collectively create more flexible coordination environments and allow for greater substitutional accommodation of rare-earth ions such as Eu^{3+}. This feature, combined with its inherent structural asymmetry, is expected to yield superior luminescence performance compared to simpler borate hosts. To the best of our knowledge, Eu^{3+} doping in LiCBO has not been previously reported nor has the effect of simultaneous Na^+/K^+ co-doping been explored in this system. Eu^{3+}-activated phosphors commonly suffer from concentration quenching and non-radiative lossesat high dopant levels, which limit their emission efficency [14]. Alkali ion co-doping has been shown to mitigate these effects by modulating the local crystal field and suppressing cross-relaxation pathways, thereby enhancing radiative transitions. Judd–Ofelt analysis further provides insight into the correlation between Eu^{3+} site symmetry, covalency, and transition probabilities, emphasizing the role of dual alkali co-doping in tailoring the luminescence behavior of LiCBO.

In this study, we present the synthesis, structural analysis, and luminescent behavior of Eu^{3+}-doped LiCBO phosphors co-doped with Na^+ and K^+ ions. The materials were synthesized via high-temperature solid-state reaction and characterized using X-ray diffraction (XRD) with Rietveld refinement, Fourier-transform infrared (FTIR) spectroscopy, and Raman spectroscopy. Rietveld refinement was employed to confirm alkali ion incorporation into the LiCBO lattice, while FTIR and Raman analyses probed local symmetry changes in the coordination environment around Eu^{3+} ions. Photoluminescence emission spectra were recorded at both room and elevated temperatures to evaluate thermal stability. Additional characterization included Judd–Ofelt intensity analysis, decay lifetime measurements, and CIE chromaticity evaluations.

This study not only advances the fundamental understanding of dual-alkali effects in borate phosphors, but also provides a compositional and spectroscopic basis for potential integration into high-efficiency red-emitting components of pc-WLED systems. Although practical device fabrication was beyond the present scope, the optical characteristics observed here demonstrate clear potential for future WLED and display applications.

2. Materials and methods

2.1. Synthesis of $LiCa_4O(BO_3)_3:Eu^{3+},Na^+,K^+$ nanophosphors

LiCBO phosphors were synthesized using a microwave-assisted sol–gel combustion method, which is well known for its efficiency in producing fine, homogeneously distributed nanomaterials. High-purity lithium carbonate (Li_2CO_3, Sigma-Aldrich, ≥99.9 %), calcium nitrate tetrahydrate ($Ca(NO_3)_2{\cdot}4H_2O$, Sigma-Aldrich, ≥99.5 %), and boric acid (H_3BO_3, Merck, ≥99 %) were used as the oxidizing precursors. Urea and glycine were added as dual fuels to promote the combustion process.

The metal precursors were weighed according to stoichiometric ratios and dissolved sequentially. Initially, Li_2CO_3 was dissolved in 1 M nitric acid under gentle heating in a quartz beaker to ensure complete dissolution. Subsequently, $Ca(NO_3)_2$ and H_3BO_3 were added to the solution and stirred in 20 mL of ultrapure water until complete clarification was achieved. After the addition of fuels, the mixture was maintained at 80 °C under continuous magnetic stirring for 1 h to promote gelation as solvent gradually evaporated.

Once a viscous gel was formed, the precursor was transferred to a microwave furnace, where rapid combustion occurred, producing a voluminous white powder with a porous morphology. To remove residual organics and improve crystallinity, the as-synthesized powder was calcined at 900 °C for 4 h in air. Europium (III) nitrate ($Eu(NO_3)_3{\cdot}xH_2O$, 99.99 %) was employed as the luminescent dopant in varying concentrations (0.5–7 wt.%), while sodium nitrate ($NaNO_3$) and potassium nitrate (KNO_3) were co-doped in corresponding ratios to investigate their influence on the emission properties. The resulting phosphors were stored in a desiccator prior to further characterization.

2.2. Characterization techniques

Phase analysis and structural characterization of the prepared LiCBO-based samples were carried out using powder X-ray diffraction (XRD) on a Malvern Panalytical Empyrean system, operating with Cu Kα radiation (λ = 1.5406 Å) over a 2θ range of 10°–80°. Rietveld refinement was performed to extract crystallographic parameters such as phase purity, lattice constants, and unit cell dimensions.

To assess the local bonding environment and structural connectivity within the borate framework, Fourier-transform infrared (FTIR) spectra were recorded using a Thermo Scientific Nicolet iS50 spectrometer, operating in the 400–4000 cm^{-1} region. Complementary structural insights were obtained from Raman spectroscopy (Renishaw inVia), with measurements conducted using a 532 nm diode laser and a 2400 lines/mm grating, spanning a spectral range of 100–2300 cm^{-1}.

Morphological and elemental analyses were performed via field-emission scanning electron microscopy (FE-SEM, JEOL JSM-7001F), coupled with energy-dispersive X-ray spectroscopy (EDS, Oxford Instruments). SEM observations were made under high vacuum with an accelerating voltage of 20 kV. A thin Au layer was sputtered onto the samples to minimize charging artifacts.

Photoluminescence (PL) emission spectra were collected using an Edinburgh Instruments FLS1000 spectrofluorometer equipped with a 150 W Xe arc lamp. Emission was monitored over the 500–750 nm range under 395 nm excitation. Time-resolved PL decay curves were also recorded to extract lifetimes. Additionally, Judd–Ofelt analysis was conducted on the room-temperature emission spectra of Eu^{3+}-doped and alkali co-doped samples to extract radiative parameters (Ω_2, Ω_4) and quantify the asymmetry of the local environment. These parameters provide valuable insight into the influence of Na^+ and K^+ ions on the crystal field distortion and hypersensitive transitions of Eu^{3+} ions.

3. Results and discussions

3.1. Phase identification and lattice refinement

The phase purity and crystal structure of undoped, Eu^{3+}-doped, and Eu^{3+}/alkali co-doped LiCBO phosphors were investigated by powder X-ray diffraction (XRD). The diffraction peaks observed for all samples were indexed to the orthorhombic phase of LiCBO (JCPDS card no. 98-009-9503), confirming successful crystallization without secondary phases. Fig. 1a displays the XRD patterns of the samples, revealing consistent phase formation across all doping conditions. The crystal structure of $LiCa_4O(BO_3)_3$ is composed of interconnected $[BO_3]$ and $[BO_4]$ units forming a three-dimensional framework with Li^+ and Ca^{2+} ions occupying interstitial and lattice sites, respectively. As shown in Fig. 1b, the larger Ca^{2+} ions (purple spheres) are distributed in the lattice positions that can be partially substituted by Eu^{3+} due to their comparable ionic radii (Ca^{2+}: 1.00 Å, Eu^{3+}: 0.95 Å in 8-coordination). The incorporation of Eu^{3+} introduces local charge imbalance, which is compensated by the presence of monovalent alkali ions (Li^+, Na^+, K^+), stabilizing the lattice and modulating the local crystal field symmetry. Rietveld refinement of the XRD data, shown in Fig. 1c, yielded lattice constants of a = 8.0916 Å, b = 9.2277 Å, and c = 3.4916 Å for the undoped composition, with a calculated unit cell volume of 260.6741

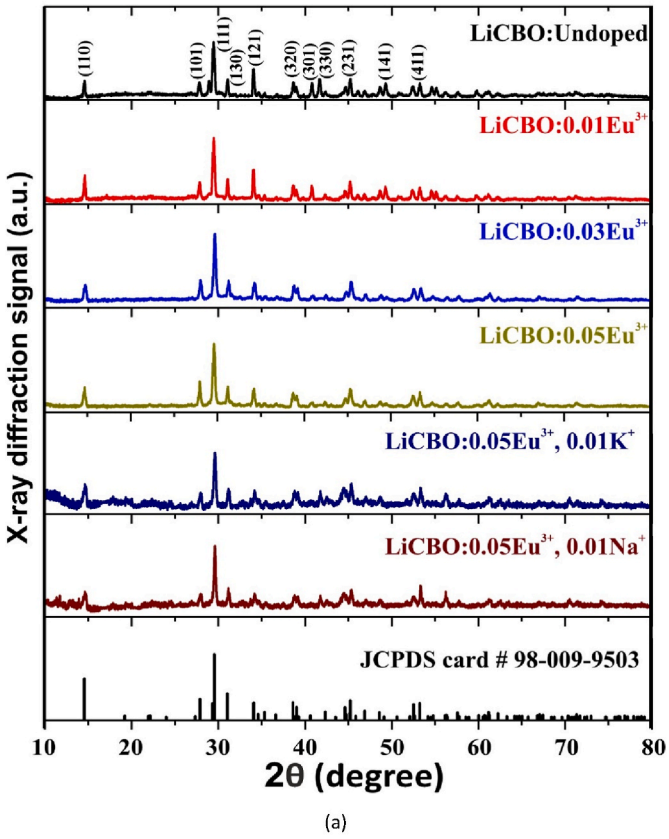

(a)

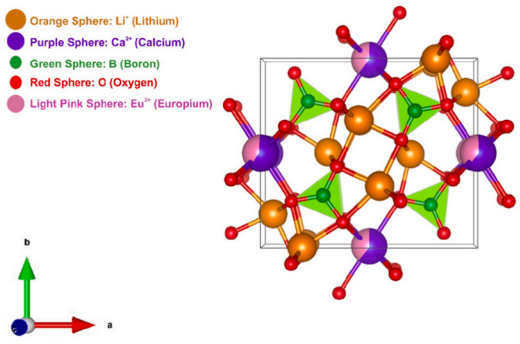

(b)

Fig. 1. (a) *Powder XRD patterns of undoped, Eu^{3+}-doped (0.01, 0.03, 0.*05 *), and Eu^{3+}/Na^{+} or K^{+} co-doped LiCBO phosphors.* (b) Crystal structure of $LiCa_4O(BO_3)_3$ showing the arrangement of Li^{+} (orange), Ca^{2+} (purple), B^{3+} (green), O^{2-} (red), and Eu^{3+} (light pink) ions. **(c)** *Rietveld refinement results for the same samples.* (For interpretation of the references to color in this figure legend, the reader is referred to the Web version of this article.)

Å^3. A summary of lattice parameters and refinement quality values for all compositions is listed in Table 1. A systematic increase in lattice volume was observed with increasing Eu^{3+} concentration (e.g., 260.89 Å^3 for 0.05 Eu^{3+}), attributed to the incorporation of Eu^{3+} ($r = 0.947$ Å) into Ca^{2+} ($r = 1.00$ Å) sites. This substitution is feasible due to their similar oxidation radii and matching oxidation states, minimizing induced lattice strain. To quantify the substitution feasibility, the ionic radius percentage difference **(D_r)** was calculated based on Shannon's method [15]:

$$D_r = \frac{|R_m(CN) - R_d(CN)|}{R_m(CN)} \times 100\% \quad (1)$$

where $R_m(CN) = 1.00$ Å (Ca^{2+}) and $R_d\ (CN) = 0.947$ Å (Eu^{3+}). The computed D_r value is 5.3 %, which is well below the typical 30 % limit for substitutional doping, confirming that Eu^{3+} can effectively occupy Ca^{2+} sites without inducing significant structural distortion. This assessment aligns with similar works, such as Gao et al. [16] on $SrAl_2O_4$: Eu^{2+} systems ($D_r \approx 0.8$ %).

Upon co-doping with Na^{+} or K^{+}, a slight decrease in unit cell volume was observed (e.g., 260.80 Å^3 for Na^{+} and 260.76 Å^3 for K^{+}), which can be attributed to local lattice distortions and charge compensation effects. The incorporation of monovalent alkali ions serves to maintain charge neutrality during $Eu^{3+} \rightarrow Ca^{2+}$ substitution and can modify the crystal field environment around Eu^{3+}, which plays a critical role in tuning the luminescent response [12].

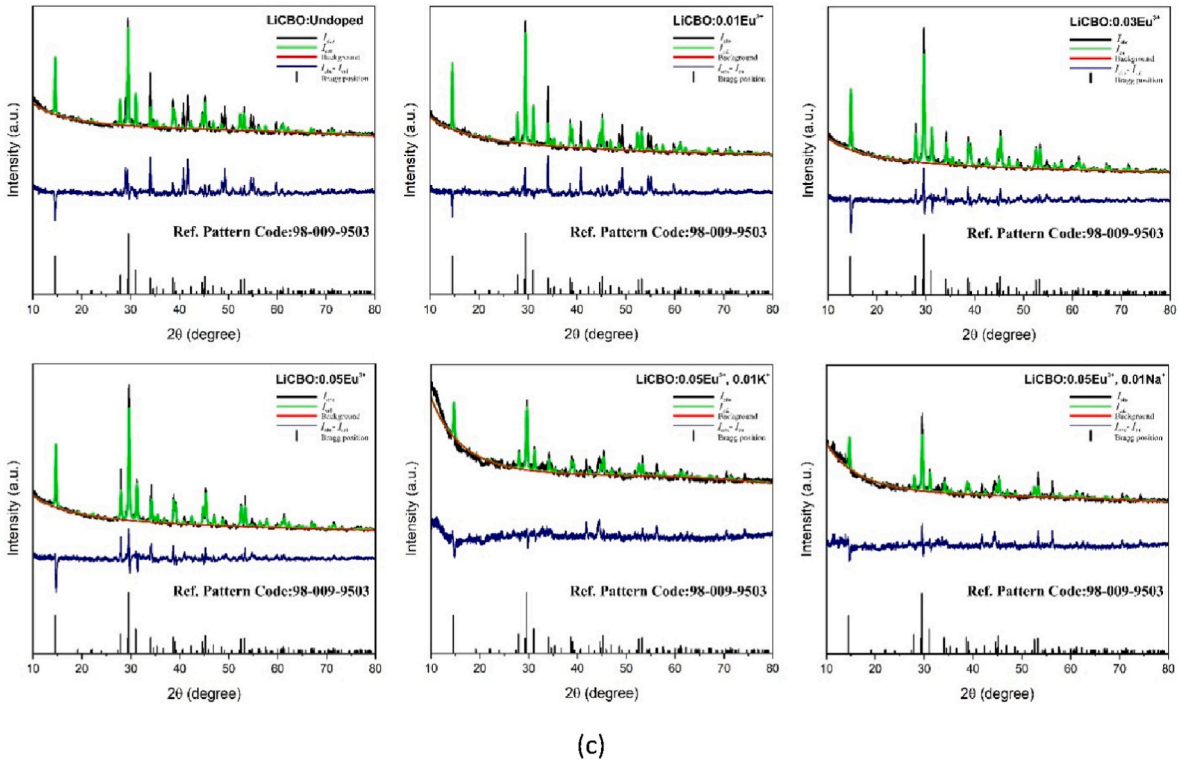

Fig. 1. (*continued*).

Table 1
Lattice parameters (a, b, c), unit cell volume, and refinement quality indicators (χ^2, R_p, R_{wp}, R_{exp}) for undoped, Eu^{3+}-doped, and Eu^{3+}/alkali co-doped LiCBO compositions.

Unit Cell	LiCBO					
	Undoped	$0.01Eu^{3+}$	$0.03Eu^{3+}$	$0.05Eu^{3+}$	$0.05Eu^{3+}$,$0.01K^{+}$	$0.05Eu^{3+}$,$0.01Na^{+}$
a [Å]	8.0916	8.0961	8.0959	8.0962	8.0965	8.0957
b [Å]	9.2277	9.2397	9.2303	9.2312	9.2300	9.2301
c [Å]	3.4916	3.4927	3.4906	3.4907	3.4893	3.4901
α, β, γ [°]	90, 90, 90	90, 90, 90	90, 90, 90	90, 90, 90	90, 90, 90	90, 90, 90
Vol. [Å^3]	260.6741	261.2776	260.8490	260.8935	260.7622	260.8012
χ^2	4.042	3.438	2.981	2.992	2.594	2.259
R_p	0.099	0.083	0.085	0.084	0.072	0.060
R_{wp}	0.152	0.129	0.118	0.118	0.091	0.080
R_{exp}	0.037	0.037	0.039	0.039	0.035	0.035

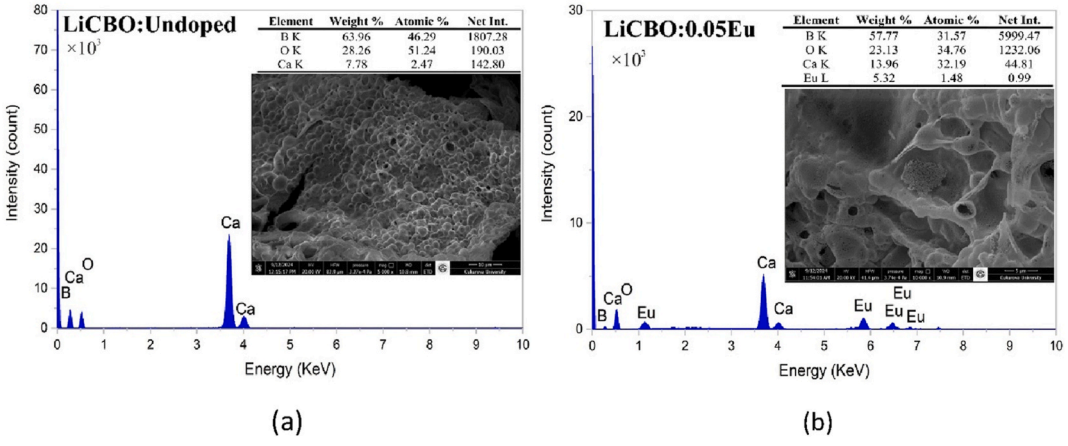

Fig. 2. SEM–EDS analysis of (a) undoped and (b) $0.05Eu^{3+}$-doped $LiCa_4O(BO_3)_3$ phosphors showing surface morphology and corresponding elemental composition.

3.2. Morphology and elemental composition

The surface morphology of the undoped and Eu^{3+}-doped LiCBO phosphors was examined using scanning electron microscopy (SEM), and the results are presented in Fig. 2.

The undoped LiCBO sample (Fig. 2 (a)) exhibits a porous and agglomerated microstructure composed of irregularly shaped grains. Such morphology is typical for borate-based phosphors synthesized via the solid-state route, reflecting incomplete grain growth and particle coalescence during sintering. Upon Eu^{3+} incorporation (Fig. 2 (b)), the morphology becomes slightly denser with fewer voids, suggesting improved grain connectivity due to enhanced diffusion during calcination.

The corresponding EDS spectra confirm the presence of the major constituent elements (Li, Ca, B, and O), consistent with the stoichiometry of the LiCBO phase. The Eu^{3+} signal in the doped sample validates the successful incorporation of europium ions into the host lattice. The elemental weight and atomic percentages (insets of Fig. 2) agree well with the expected composition, indicating phase purity and uniform dopant distribution within the analyzed region.

3.3. Microstructural analysis and crystallite size estimation

The microstructural characteristics of the undoped, Eu^{3+}-doped, and Eu^{3+}/alkali co-doped LiCBO samples were analyzed through X-ray diffraction line-broadening using several complementary models, namely the Debye–Scherrer, Monshi–Scherrer, Williamson–Hall (W-H), Halder–Wagner (H–W), and Size–Strain Plot (SSP) methods. These approaches provide complementary insights into crystallite size and lattice strain by accounting for different contributions to peak broadening including instrumental effects, microstrain, and crystallite geometry [17–19].

Fig. 3a–c shows the W-H, H-W, and SSP plots, respectively, for selected compositions. All three models exhibit positive slopes, indicating the coexistence of crystallite size and microstrain contributions. All four methods are consistent in trend, showing a decrease with Na^+/K^+ co-doping, with H–W giving the largest D and SSP providing a balanced estimate; critically, the W–H and H–W slopes confirm a systematic increase in ε with alkali co-doping. Fig. 3d illustrates the linear fitting obtained from the Monshi–Scherrer approach [20], which modifies the standard Scherrer formula to account for Gaussian peak profiles. The results are consistent with other size estimation methods, especially for low Eu^{3+} concentrations. As shown in Fig. 3e, the comparative grain size trends obtained from all models highlight a clear decrease in crystallite size upon alkali co-doping. For example, the 0.05 Eu^{3+}-doped sample exhibited a peak crystallite size of 86.71 nm (H-W method), which reduced to 64.65 nm for the 0.05 Eu^{3+}/0.01 Na^+ sample. Consistent size reduction across models, together with higher ε values, indicates that line broadening is dominated by strain introduced by alkali-induced lattice distortions; any additional reduction from growth inhibition during synthesis is likely secondary under our identical calcination conditions. The corresponding strain values (ε), summarized in Table 2, show a noticeable increase in co-doped samples compared to Eu^{3+}-only doped ones. For instance, ε increased from 2.32×10^{-3} for 0.05 Eu^{3+} to 3.02×10^{-3} for Na^+ co-doping (W-H method), suggesting enhanced microstrain due to charge compensation mechanisms and ionic radius mismatch. This strain increase correlates with inhibited crystallite growth, a behavior similarly reported for other rare-earth-doped systems under co-doping conditions [21,22].

3.4. Fourier-transform infrared (FTIR) spectroscopy

FTIR spectroscopy was performed to examine the structural evolution of Eu^{3+}-doped LiCBO phosphors, both with and without alkali metal co-doping (Fig. 4). The spectra, recorded in the range of 400–1600 cm^{-1} exhibit characteristic vibrational bands of borate structures, providing insights into the local coordination and network connectivity within the host matrix. The strongest band at approximately 1424 cm^{-1} is assigned to the asymmetric stretching vibrations of trigonal BO_3 units, which dominate in metaborate-type lattices. The adjacent band at 1206 cm^{-1} corresponds to B_3–O stretching vibrations associated withlinkages in more complex borate rings or chains [23,24]. A pronounced absorption band centered at 919 cm^{-1} is attributed to the stretching of tetrahedral BO_4 units, indicating the partial conversion of BO_3 to BO_4 species and the coexistence of mixed borate coordination. Additional shoulders at 815 cm^{-1} and 757 cm^{-1} further confirm the presence of a polymerized borate network [25]. Lower frequency peaks at 654 cm^{-1} and 452 cm^{-1} correspond to B–O–B bending modes, reflecting the cross-linking and angular deformations between borate units. These modes are highly sensitive to structural rearrangements, particularly in the presence of alkali modifiers [9]. Minor shifts andintensity variations in the 900–500 cm^{-1} region (especially for the B–O–B bending at ~654 and 452 cm^{-1}) suggest network reorganization under Na^+ co-doping; this correlates with enhanced even-rank (k = 4) crystal-field terms that favor the $^5D_0 \rightarrow {}^7F_4$ emission. Co-doping with Na^+ and K^+ enhances the bending mode intensities, indicating variations in local field strength and network modification. Similar effects have been reported in rare-earth-doped borate systems containing alkali ions [26]. These FTIR observations are in good agreement with the structural data obtained from XRD and Rietveld refinement. The coexistence of BO_3 (1424, 1206 cm^{-1}) and BO_4 (~919 cm^{-1}) units confirms the formation of a mixed borate framework. In Na^+-co-doped samples, subtle intensity and position variations of these bands suggest an increased proportion of BO_4-linked environments and enhanced B–O–B connectivity, consistent with a higher-rank crystal field around Eu^{3+}. Furthermore, the slight band shifts and intensity variations induced by Eu^{3+} and alkali ion doping correspond well with the measured changes in lattice parameters and unit cell volumes from Rietveld analysis, further confirming the successful substitution and its influence on the local structure. The intensified B–O–B bending modes at 654 and 452 cm^{-1} also correlate with increased microstrain and structural distortion suggested by XRD peak broadening. These correlations collectively confirm the structural integrity of the doped borate system and emphasize the role of modifying ions in the network framework.

3.5. Raman spectroscopy analysis

The Raman spectra of LiCBO:Eu^{3+} samples exhibit distinct bands in the range of 1450–2700 cm^{-1}, which are mainly attributed to the internal vibrational modes of the borate network. The undoped sample displays broad bands centered at approximately 1545, 1784, 1893, 1978, 2408, 2413, 2493, and 2682 cm^{-1} as shown in Fig. 5. These bands are characteristic of both symmetric and asymmetric stretching vibrations of trigonal BO_3 and tetrahedral BO_4 units, in agreement with previously reported borate Raman features [25,27]. Upon doping with Eu^{3+} ions, significant enhancement and narrowing of these peaks is observed, particularly in the region between 1450 and 2000 cm^{-1}, which suggests improved crystallinity and a more ordered short-range structure within the borate framework. This effect is most pronounced for the sample doped with 0.05 Eu^{3+}, implying that this concentration induces optimal local structural rearrangement, as similarly reported in Eu^{3+}-doped silica borate glass systems [28]. In Na^+-co-doped samples, the broader Raman features (1450–2000 cm^{-1}) indicate local disorder and redistribution of BO_3/BO_4 units. Such symmetry lowering around Eu^{3+} sites is consistent with enhanced Ω_4-dominated crystal-field contributions and the observed inversion of the transition intensities ($^5D_0 \rightarrow {}^7F_4 > {}^5D_0 \rightarrow {}^7F_2$).

These observations correlate well with FTIR and XRD results, confirming the coexistence of mixed BO_3–BO_4 units and underscoring the role of Eu^{3+} and alkali modifiers in tuning the structural order of the borate host matrix. The FTIR findings are further corroborated by Raman spectroscopy, which reveals enhanced vibrational features and

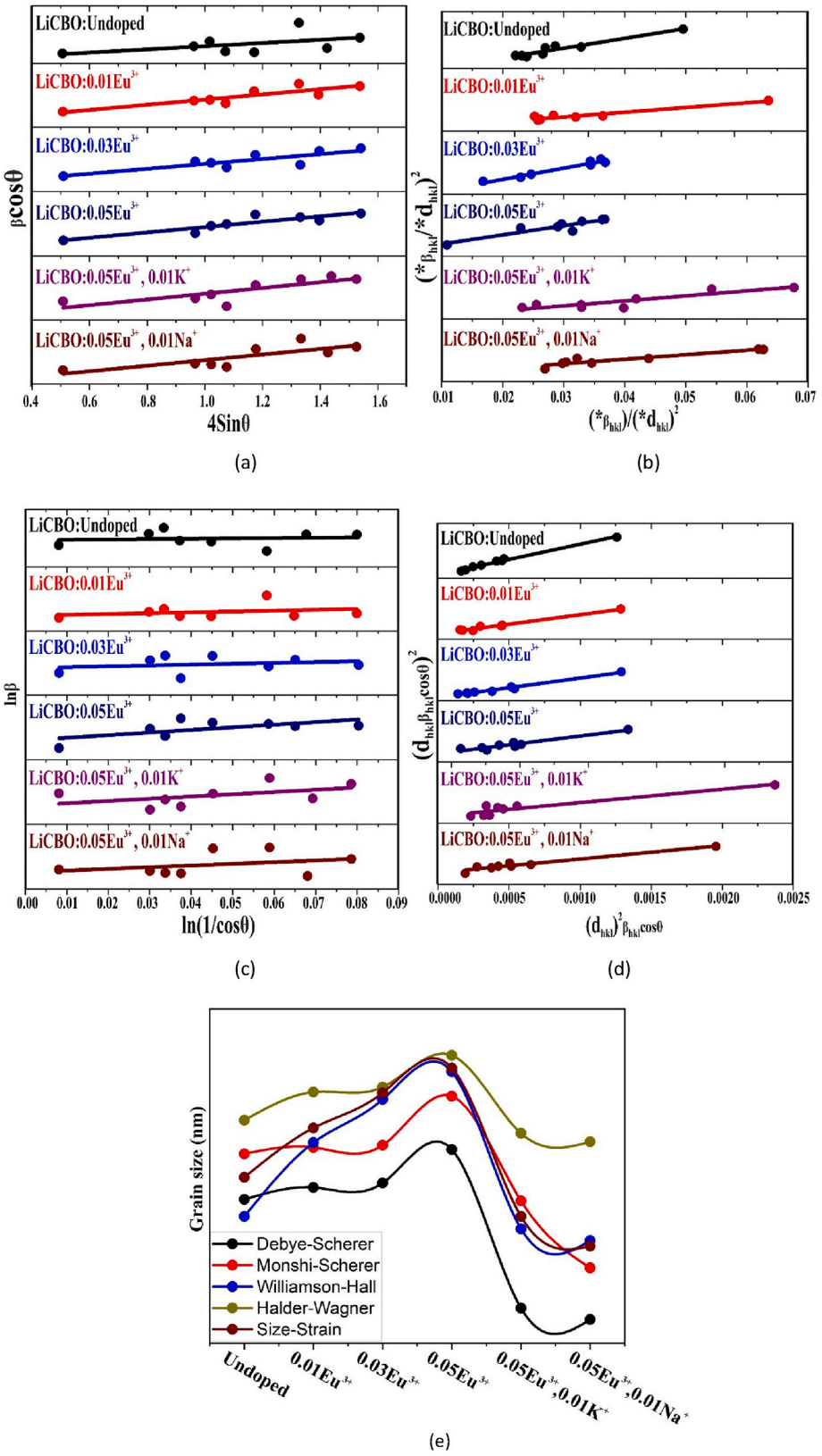

Fig. 3. (a) Williamson–Hall plots showing the relationship between 4sinθ and βcosθ for various LiCBO compositions. (b) Halder–Wagner plots derived from XRD data, used to evaluate crystallite size and strain contributions. (c) Monshi–Scherrer plots depicting ln(1/cosθ) versus lnβ for different doping levels. (d) Size–Strain Plot (SSP) analyses demonstrating strain and size effects through $\left(d_{hkl}^2\beta_{hkl}\cos\theta\right)^2$ vs $\left(d_{hkl}^2\cos\theta\right)$ representations. (e) Comparative grain size evaluation of all samples using Debye–Scherrer, Monshi–Scherrer, W-H, H–W, and SSP models, highlighting the effects of Eu^{3+} doping and alkali co-doping on crystallite size trends.

Table 2
Crystallite size (D) and microstrain (δ, ε) parameters of LiCBO: xEu^{3+} and alkali co-doped samples, calculated using Debye–Scherrer, Monshi–Scherrer, Williamson–Hall, Halder–Wagner, and Size–Strain models.

Concentration		Undoped	$0.01Eu^{3+}$	$0.03Eu^{3+}$	$0.05Eu^{3+}$	$0.05Eu^{3+}$,$0.01K^{+}$	$0.05Eu^{3+}$,$0.01Na^{+}$
Debye-Scherer	D (nm)	68.227	69.903	70.525	75.249	52.920	51.329
	$\delta \times 10^{-3}$ (nm^{-2})	0.2148	0.2046	0.2010	0.1766	0.3570	0.3795
Monshi-Scherrer	D (nm)	74.642	75.543	75.846	82.740	68.013	58.598
	$\delta \times 10^{-3}$ (nm^{-2})	0.1794	0.1755	0.1738	0.1460	0.2161	0.2912
Williamson-Hall	D (nm)	65.825	76.219	82.282	86.200	64.078	62.420
	$\varepsilon \times 10^{-3}$	2.21	2.24	2.12	2.32	2.98	3.02
Halder-Wagner	D (nm)	79.365	83.333	84.033	88.495	77.519	76.335
	$\varepsilon \times 10^{-3}$	11.00	10.61	10.31	9.28	1.26	13.93
Size-Strain	D (nm)	71.338	78.279	83.227	86.716	65.825	64.650
	$\varepsilon \times 10^{-3}$	1.78	1.67	1.51	2.09	2.17	1.92

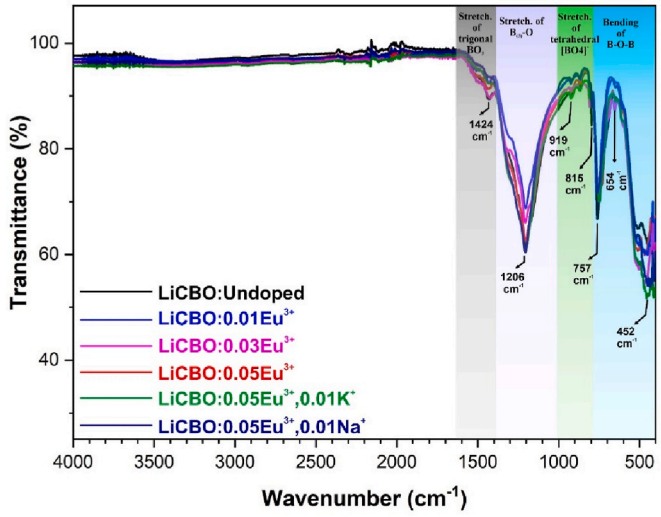

Fig. 4. FTIR spectra of LiCBO:Eu^{3+} phosphors co-doped with Na^{+} and K^{+}, showing characteristic bands of BO_3 and BO_4 units.

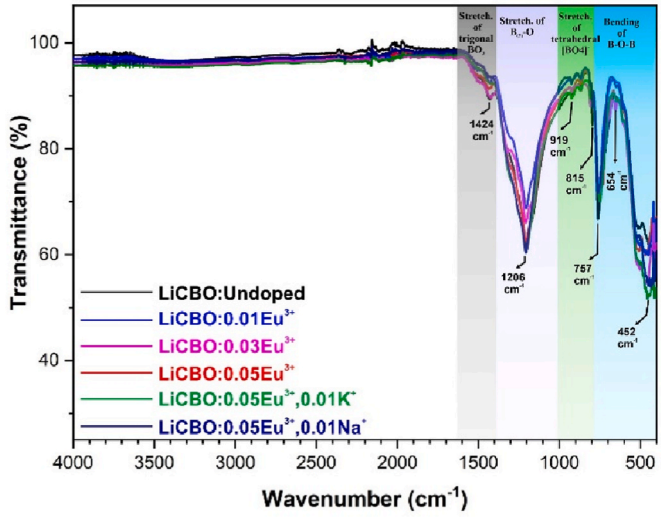

Fig. 5. Raman spectra of LiCBO:Eu^{3+} phosphors with varying dopant and co-dopant concentrations, showing characteristic vibrational modes of BO_3 and BO_4 units.

improved structural organization upon Eu^{3+} doping, particularly for the 0.05 composition. The strong agreement between the FTIR and Raman analysis verifies the coexistence of BO_3 and BO_4 units and provides compelling evidence for the successful incorporation of dopant and co-dopant ions into the borate network.

3.6. Steady-state photoluminescence

The excitation and emission behavior of Eu^{3+}-doped LiCBO was investigated to assess its optical response. Fig. 6 depicts the excitation spectrum monitored at 613 nm emission, together with the corresponding emission spectrum under 393 nm excitation.

The excitation spectrum shows a broad CT band at 299 nm ($O^{2-} \rightarrow Eu^{3+}$), typical of Eu^{3+}-doped borates [5]. The position of this CTB is strongly influenced by the local coordination environment of Eu^{3+} ions. In borate lattices, the coexistence of BO_3 and BO_4 units provides an asymmetric ligand field around Eu^{3+}, leading to a CTB position slightly shifted compared to other oxide hosts. The broad CT band suggests Eu–O bond length variation due to BO_3/BO_4 disorder. This assignment is consistent with previous studies, where the CTB location was shown to correlate with Eu–O bond lengths and the relative proportion of BO_3/BO_4 groups in the host structure [5,6]. In addition, multiple sharp intra-4f transitions of Eu^{3+} are observed, including $^7F_0 \rightarrow {}^5H_6$ (319 nm), $^7F_0 \rightarrow {}^5D_4$ (361 nm), $^7F_0 \rightarrow {}^5L_7$ (382 nm), $^7F_0 \rightarrow {}^5L_6$ (393 nm), $^7F_0 \rightarrow {}^5D_3$ (413 nm), and $^7F_0 \rightarrow {}^5D_2$ (465 nm). These characteristic excitation lines are in good agreement with previous reports on Eu^{3+}-activated borate phosphors [6,13]. Among these, the intense excitation peak at 393 nm is of particular importance as it falls within the near-UV emission range of commercial GaN-based LEDs, rendering the material a suitable candidate for pc-WLED applications. This spectral overlap with the near-UV GaN emission ensures efficient excitation–emission coupling, a prerequisite for high-performance pc-WLED phosphors [29,30]. Comparable

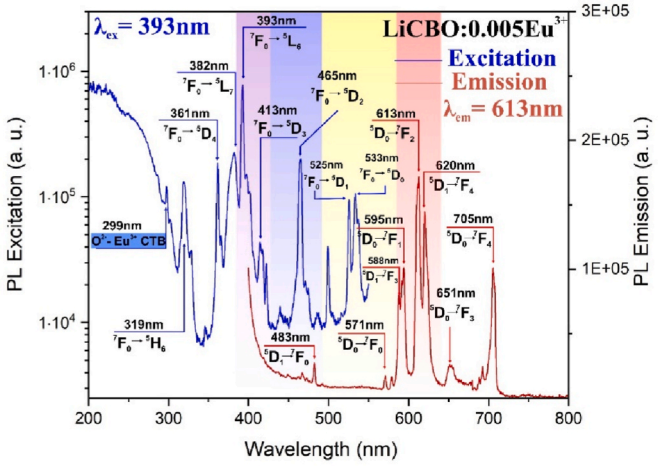

Fig. 6. Excitation (λ_{em} = 613 nm) and emission (λ_{ex} = 393 nm) spectra of LiCBO:0.5 wt% Eu^{3+} phosphor, showing the $O^{2-} \rightarrow Eu^{3+}$ charge transfer band and characteristic f–f transitions dominated by the red $^5D_0 \rightarrow {}^7F_2$ emission at 613 nm. (For interpretation of the references to color in this figure legend, the reader is referred to the Web version of this article.)

results have been reported not only in Eu^{3+}-activated borate phosphors [2,5,13], but also in other host matrices such as perovskites and oxides, where 393 nm excitation efficiently drives strong red emission [29,30].

Upon 393 nm excitation, the emission spectrum of Eu^{3+}-doped LiCBO is dominated by the characteristic 4f–4f transitions. The most intense red emission is assigned to the hypersensitive electric dipole $^5D_0 \rightarrow {}^7F_2$ transition at 613 nm, which is strongly influenced the local crystal field symmetry surrounding Eu^{3+} ions. The dominance of the $^5D_0 \rightarrow {}^7F_2$ transition over the magnetic dipole $^5D_0 \rightarrow {}^7F_1$ (595 nm) transition indicates that Eu^{3+} ions predominantly occupy non-centrosymmetric sites within the LiCBO lattice. Additional emission lines are observed at 588 nm ($^5D_0 \rightarrow {}^7F_3$), 620 and 705 nm ($^5D_0 \rightarrow {}^7F_4$), 651 nm ($^5D_0 \rightarrow {}^7F_3$), along with a weak feature at 483 nm ($^5D_1 \rightarrow {}^7F_0$). The presence of multiple Stark-split components further confirms the crystalline environment of Eu^{3+} sites in LiCBO matrix.

Although the 613 nm line ($^5D_0 \rightarrow {}^7F_2$) is the strongest peak ($I_{613}/I_{595} \approx 1.7$), integrated intensity shows the $^5D_{1,0} \rightarrow {}^7F_4$ manifold (620 and 705 nm) dominates $I(^7F_4)/I(^7F_1) \approx 3.0$ and $I(^7F_4)/I(^7F_2) \approx 4.6$. This apparent discrepancy arises because the $^7F_2$ emission is relatively sharp and concentrated in a narrow spectral region, whereas $^7F_4$ is distributed over multiple Stark sublevels, resulting in a broad band with a larger integrated oscillator strength. This behavior suggests that Ω_4 is dominant, reflecting stronger Eu–O covalency and a more rigid coordination field. It should be emphasized that although the integrated intensity of the $^5D_0 \rightarrow {}^7F_4$ manifold is higher, the sharp $^5D_0 \rightarrow {}^7F_2$ transition dominates the perceived red emission due to its strong peak intensity and spectral localization around 613 nm.

The narrow and intense 613 nm emission LiCBO:Eu^{3+} as a promising red phosphor for high color-purity applications. Moreover, the asymmetry ratio $R = I_{613}/I_{595}$ provides a quantitative measure of site distortion, consistent with the orthorhombic asymmetry revealed by structural analysis. These observations align with previous reports on Eu^{3+}-activated borates, where lattice distortion and alkali co-doping were shown to significantly enhance red emission intensity [2,5,13]. Taken together, the spectral features confirm that Eu^{3+}-activated LiCBO phosphors exhibit efficient red luminescence under near-UV excitation, making them promising candidates for solid-state lighting applications. Judd–Ofelt analysis (Section 3.6.4) was employed to determine the intensity parameters Ω_2, Ω_4, Ω_6, along with the branching ratios (β_J), to gain deeper insight into the local environment of Eu^{3+} ions. In particular, Ω_2 is expected to correlate with the asymmetry ratio (R), reflecting variations in site symmetry, whereas the enhanced intensity of the $^7F_4$ transition is anticipated to be associated with elevated Ω_4 values., Together, these parameters provide a robust quantitative framework for interpreting the emission mechanism.

3.6.1. *Effect of Eu^{3+} concentration on photoluminescence*

The emission spectra of LiCBO:xEu^{3+} (x = 0.5–7 wt%) under 393 nm excitation (Fig. 7) exhibit the typical rise–maximum–fall behavior: the integrated red emission increases with Eu^{3+} loading and reaches an optimum at 5 wt%, followed by a decrease due to concentration quenching. This trend reflects non-radiative energy transfer among neighbouring Eu^{3+} ions once a critical dopant spacing is exceeded, a mechanism widely reported for Eu^{3+}-activated borates [13,31,32].

A salient feature of LiCBO is the delayed onset of quenching at 5 wt %, which is comparatively high among borate hosts and indicates that the mixed BO_3/BO_4 network can accommodate substantial Eu^{3+} contents before energy migration losses dominate [32,33]. At low concentrations (≤2 wt%), the hypersensitive $^5D_0 \rightarrow {}^7F_2$ (613 nm) line grows faster than the magnetic-dipole $^5D_0 \rightarrow {}^7F_1$ (595 nm), evidencing preferential occupation of non-centrosymmetric sites; the asymmetry ratio $R = I_{613}/I_{595}$ peaks near 5 wt% and then declines as cross-relaxation and migration to quenching centers set in, while the line pattern remains essentially unchanged. Similar concentration-dependent behavior was also observed under alternative excitation wavelengths corresponding to other Eu^{3+} intra-4f transitions (319, 361, 382, and 465 nm), where the emission spectra likewise exhibited an increase up to 5 wt% Eu^{3+} followed by concentration quenching. This consistency across different excitation channels confirms that the quenching behavior is an intrinsic feature of Eu^{3+}–Eu^{3+} interactions in the LiCBO host rather than being strongly dependent on the excitation pathway.

To rationalize the quenching threshold, we estimated the critical transfer distance using Blasse's relation [34]:

$$R_c = 2\left[\frac{3V}{4\pi x_c N}\right]^{1/3} \quad (2)$$

where V is the unit-cell volume, x_c is the critical Eu^{3+} site fraction, and N

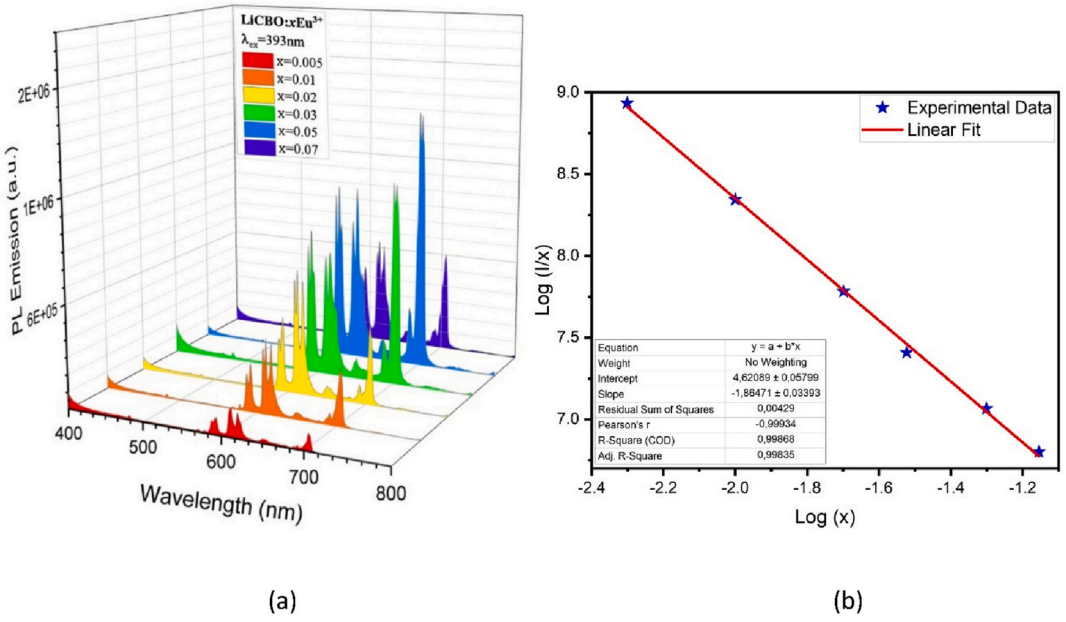

Fig. 7. (a) Emission spectra of LiCBO:xEu^{3+} (x = 0.005–0.07) phosphors under 393 nm excitation, showing the evolution of characteristic Eu^{3+} transitions with dopant concentration. (b) Log–log plot of integrated emission intensity vs. Eu^{3+} concentration fitted with the Dexter energy transfer model, used to estimate the critical distance and interaction mechanism.

is the number of Eu-substitutable cation sites per unit cell. From Rietveld refinement at 5 wt% Eu^{3+}, we use V = 260.89 $Å^3$. The nominal 5 wt% Eu^{3+} corresponds to a site (atomic) fraction of ~3.3 at. % for Eu substituting Ca^{2+}. Since each formula unit contains one Ca^{2+} site and LiCBO crystallizes with Z = 4, there are N = 4 available substitution sites per unit cell. Substituting these values R_c is found to be ~14 Å . Because $R_c \gg 5$ Å, exchange interactions can be excluded, and concentration quenching is governed by multipolar (predominantly dipole–dipole) energy transfer, consistent with the Dexter mechanism [35] and with observations in related borate phosphors [32,36].

To elucidate the quenching mechanism, the relationship between luminescence intensity (I) and activator concentration (x) was analyzed according to the Dexter–Inokuti model using the equation:

$$log\left(\frac{I}{x}\right) = -\frac{\theta}{3}log(x) + c \quad (3)$$

where θ = 6, 8, and 10 correspond to dipole–dipole, dipole–quadrupole, and quadrupole–quadrupole interactions, respectively [35]. In the present case, concentration quenching becomes evident beyond 5 wt% Eu^{3+}, and regression of the quenching region (x = 0.05–0.07) yields a slope of −1.93, corresponding to θ ≈ 6. This value indicates that dipole–dipole interactions dominate the non-radiative energy transfer process, consistent with the exclusion of exchange interactions derived from the critical distance $R_c \gg$ 5Å Although the quenching region is represented by only three concentration points, limiting statistical robustness, the obtained θ ≈ 6 indicates a dipole–dipole dominated quenching mechanism. This interpretation is further supported by previous studies in Eu^{3+}-doped systems—for example, in oxyfluoroborate glasses where the quenching mechanism was confirmed as dipole–dipole [37], in $Ba_2Lu_5B_5O_{17}$ where the critical distance and mechanism align with dipole–dipole energy transfer [38], and more recently in borate phosphors where high Eu^{3+} solubility and concentration quenching were also attributed to multipolar interactions [39]. Overall, LiCBO shows a high quenching threshold (5 wt%) and retains strong red emission up to this loading, underscoring the robustness of its borate framework for high-activator formulations in solid-state lighting. In the next section, we quantify these trends via area-based branching ratios and Judd–Ofelt parameters, providing a consistent link between the observed intensity evolution and local symmetry/covalency effects.

3.6.2. *Effect of alkali ion (Na^+, K^+) co-doping on the emission behavior*

The luminescence of LiCBO:0.05Eu^{3+} was examined under varying Na^+ and K^+ concentrations (Fig. 8). In both cases, emission followed a rise–maximum–fall trend, peaking at y = 0.01. The enhancement at low alkali levels arises from charge compensation, which reduces defects and favors energy transfer to Eu^{3+}. Beyond this point, excess alkali incorporation likely introduces additional structural disorder, resulting in non-radiative pathways and quenching of emission. Such charge-compensation effects are associated with the incorporation of monovalent alkali ions (Li^+, Na^+, K^+) that balance the excess positive charge generated when Eu^{3+} substitutes for Ca^{2+} in the $LiCaBO_3$ lattice. This process suppresses the formation of oxygen vacancies and other defect centers, thereby reducing nonradiative recombination and improving the energy transfer efficiency to Eu^{3+} ions. A similar mechanism has been reported in $Ca_2Al_2SiO_7$:Eu^{3+} phosphors, where Li^+, Na^+, and K^+ co-doping significantly enhanced emission intensity by charge compensation [40]. The positive effect of alkali incorporation on luminescence enhancement through charge balancing was also observed in Eu^{3+}-activated lithium borates and oxyborates [41] and in Li^+/K^+ co-doped ZnO:Eu^{3+} systems [42], confirming that controlled alkali substitution effectively reduces defect-related quenching and stabilizes the local crystal field around Eu^{3+} ions.

A key distinction is that, while both ions enhance the 613 nm emission at low level, Na^+ co-doping at y = 0.01 causes the 705 nm ($^5D_0 \rightarrow {}^7F_4$) transition to exceed the 613 nm ($^5D_0 \rightarrow {}^7F_2$) line by ~1.5-fold. Such inversion of peak dominance is highly unusual for Eu^{3+}-activated borates, where the $^5D_0 \rightarrow {}^7F_2$ transition is typically strongest due to its hypersensitive character.

This inversion is consistent with the FTIR and Raman evidence indicating BO_3/BO_4 redistribution under Na^+ co-doping. The increased BO_4- connectivity and modified B–O–B bending enhance the even-rank crystal-field components (k = 4) at Eu^{3+} sites, thereby redistributing oscillator strength toward $^5D_0 \rightarrow {}^7F_4$ transition. Similar effects of alkali modification on Eu^{3+} emission distribution have been reported in other oxide hosts, where Na^+ was shown to induce notable changes in multipolar interactions and site symmetry [13,43].

In contrast, K^+ co-doping does not lead to such spectral inversion; instead, it primarily enhances the overall red emission without significantly altering the relative balance of the $^5D_0 \rightarrow {}^7F_2$ and $^5D_0 \rightarrow {}^7F_4$ transitions. This difference highlights the stronger field perturbation induced by the smaller Na^+ ion compared to K^+, consistent with its higher tendency to distort the Eu^{3+} coordination environment.

Taken together, these findings demonstrate that alkali ion co-doping not only governs the intensity of Eu^{3+} emission but also enables the controlled modulation of the spectral distribution of Eu^{3+} transitions in borate phosphors. Such modulation arises from alkali-induced changes in the local crystal field symmetry and covalency around Eu^{3+} centers, which influence the relative intensity of the hypersensitive ($^5D_0 \rightarrow {}^7F_2$) and magnetic-dipole ($^5D_0 \rightarrow {}^7F_1$) transitions. Similar spectral tuning and charge-compensation effects of alkali incorporation have been reported in Eu^{3+}- and Sm^{3+}-activated phosphate systems synthesized by wet chemical routes [44–46]. In particular, Na^+ emerges as a powerful modifier capable of tuning the spectral balance between the hypersensitive and higher-order transitions, offering new opportunities for the

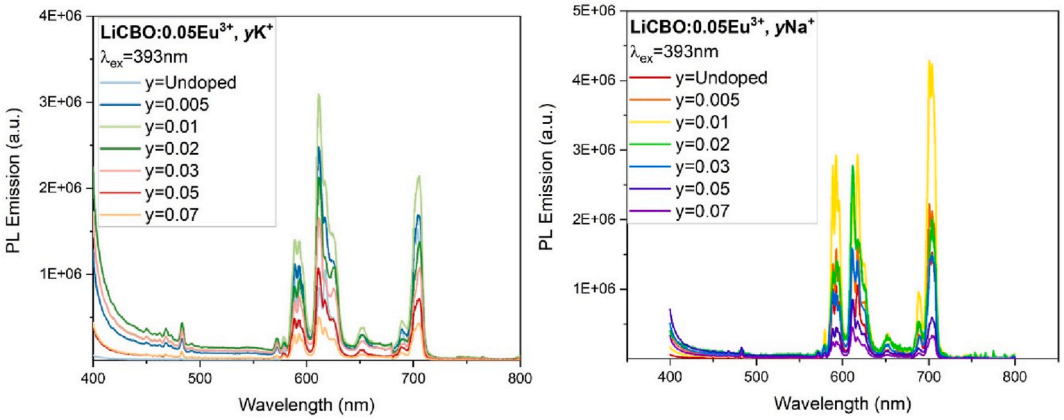

Fig. 8. PL emission spectra of LiCBO:0.05Eu^{3+} co-doped with (a) K^+ and (b) Na^+ under 393 nm excitation as a function of co-dopant concentration.

design of wavelength-tailored red phosphors for solid-state lighting applications.

3.6.3. Fluorescence lifetime analysis

The decay profiles of LiCBO:Eu^{3+} with and without alkali co-doping were recorded under 393 nm excitation and monitored at 613 nm (Fig. 9). All curves can be satisfactorily fitted with a bi- or tri-exponential function, indicating the presence of multiple decay channels associated with distinct Eu^{3+} environments. The corresponding parameters are summarized in Table 3. For the singly doped samples, the average lifetime (τ_{avg}) increases with Eu^{3+} concentration up to 0.05, reaching ~1.31 ms, consistent with reduced quenching and more efficient energy migration among sensitized centers. A more complex trend emerges with alkali co-doping. At low levels (y = 0.01), both K^+ and Na^+ drastically shorten τ_{avg} (~0.59 ms and ~0.52 ms, respectively). Although counterintuitive, this behavior arises from insufficient alkali incorporation, which causes incomplete charge compensation and local lattice distortions. These perturbations generate defect-related non-radiative centers that accelerate energy dissipation, resulting in unusually short decay times. Similar effects of charge imbalance and defect-mediated quenching in Eu^{3+} systems have been reported by Chatterjee et al. [47] for K^+ co-doped $BaAl_2O_4$:Eu^{3+} and by Bhagyalekshmi and Rajendran [48] in Eu^{3+}-activated spinel titanates. At higher alkali concentrations (y = 0.03), the average lifetimes increase markedly to 2.16 ms (K^+) and 2.48 ms (Na^+). This pronounced enhancement suggests that optimal alkali substitution effectively neutralizes charge imbalance, reduces defect density, and stabilizes Eu^{3+} sites through local charge compensation and structural relaxation. The result is a suppression of non-radiative channels and extension of the Eu^{3+} radiative lifetime. Overall, the lifetime evolution highlights the dual role of alkali co-doping: at low levels it generates non-radiative defects, whereas at optimized concentrations it stabilizes the Eu^{3+} environment and extends the lifetime.

3.6.4. Judd–Ofelt analysis

The Judd–Ofelt (J–O) formalism was employed to quantify the radiative properties of Eu^{3+} in LiCBO:0.05Eu^{3+} and its alkali-co-doped derivatives. The theoretical framework was originally proposed by Judd [49] and Ofelt [50], and the reduced matrix elements $\langle U^{(\lambda)}\rangle^2$ were taken from the tabulated values of Carnall et al. [51]. The emission spectra were resolved into the $^5D_0 \rightarrow {}^7F_J$ (J = 1–4) manifolds, and the experimental branching ratios were calculated from the area-integrated intensities according to

$$\beta_J^{exp} = \frac{I_J \tilde{\nu}_J^3}{\sum_K I_K \tilde{\nu}_K^3} \tag{4}$$

where $\tilde{\nu}_J = 1/\lambda_J$ is the mean transition wavenumber. The magnetic-dipole transition $^5D_0 \rightarrow {}^7F_1$ was adopted as an internal reference with $A_{MD} = 14.65 n^3\ s^{-1}$ (n = 1.8), allowing absolute radiative rates to be determined as $A_{tot} = A_{MD}/\beta_1$. The corresponding branching fractions, transition rates, and lifetimes are summarized in Table 4.

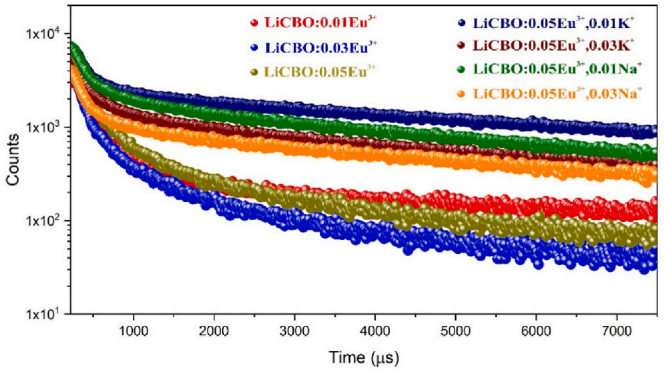

Fig. 9. Photoluminescence decay curves of Eu^{3+} emission at 613 nm for LiCBO: xEu^{3+} with different doping concentrations and co-doping conditions (K^+, Na^+) under 393 nm excitation.

Table 3
Fitted decay parameters (τ_1, τ_2, τ_3), relative contributions, average lifetime (τ_{avg}), and fitting quality (χ^2) for Eu^{3+} emission in LiCBO: xEu^{3+} and alkali co-doped samples.

		Time(ms)	Rel.%	τ_{avg}(ms)	χ^2
LiCBO:0.01Eu^{3+}	τ_1	0.01	16.57	0.70	1.35
	τ_2	0.67	14.80		
	τ_3	0.94	68.63		
LiCBO:0.03Eu^{3+}	τ_1	0.01	37.10	1.29	1.19
	τ_2	0.49	28.55		
	τ_3	2.10	34.35		
LiCBO: 0.05Eu^{3+}	τ_1	0.01	29.46	1.31	1.15
	τ_2	0.42	29.96		
	τ_3	2.06	40.58		
LiCBO:0.05Eu^{3+},0.01K^+	τ_1	0.01	4.78	0.59	1.17
	τ_2	0.73	3.97		
	τ_3	0.56	91.25		
LiCBO:0.05Eu^{3+},0.03K^+	τ_1	0.01	19.14	2.16	1.38
	τ_2	2.21	80.86		
LiCBO:0.05Eu^{3+},0.01Na^+	τ_1	0.01	7.13	0.51	1.07
	τ_2	0.63	7.65		
	τ_2	0.45	85.2		
LiCBO:0.05Eu^{3+},0.03Na^+	τ_1	0.01	15.40	2.48	1.23
	τ_2	2.52	84.6		

The Eu-only sample displays a spectral distribution dominated by the $^5D_0 \rightarrow {}^7F_4$ emission ($\beta_4 \approx 0.48$), yielding a moderate total radiative rate ($A_{tot} = 2.63 \times 10^2\ s^{-1}$) and a radiative lifetime of 3.81 ms. Incorporation of K^+ ions produces a strong redistribution of oscillator strength toward the hypersensitive $^5D_0 \rightarrow {}^7F_2$ transition ($\beta_2 \sim 0.60$), increasing the overall radiative rate ($A_{tot} = 6.72 \times 10^2\ s^{-1}$) and reducing the lifetime of 1.49 ms. By contrast, Na^+ co-doping leaves the branching pattern nearly unchanged relative to Eu-only, with the $^5D_0 \rightarrow {}^7F_4$ manifold still prevailing and τ_{rad} close to 3.78 ms.

The asymmetry ratio $= I_{613}/I_{595}$, the measured decay times, and the resulting internal quantum efficiencies are listed in Table 5. The pronounced increase of R in the K^+ sample (R ≈ 5.15) reflects a strongly distorted and non-centrosymmetric local environment around Eu^{3+}, which favors electric-dipole transitions. This interpretation is consistent with the higher radiative rate and improved efficiency (~40 %). Conversely, Na^+ incorporation produces only a marginal increase in R while simultaneously reducing the efficiency to ~14 %, suggesting that that phonon-assisted non-radiative channels are enhanced in this case [52].

The J–O intensity parameters were further analyzed using Carnall's reduced matrix elements.

The spontaneous emission probability for an electric-dipole transition is expressed as

$$A_J^{ED} = \frac{64\pi^4 e^2}{3h(2J_i+1)c^3} \cdot \frac{n(n^2+2)^2}{9} \cdot \tilde{\nu}_J^3 \cdot S_{ed}(J) \tag{5}$$

where the line strength is given by

$$S_{ed}(J) = \Omega_2 \langle U^{(2)}\rangle^2 + \Omega_4 \langle U^{(4)}\rangle^2 + \Omega_6 \langle U^{(6)}\rangle^2 \tag{6}$$

For completeness, the transition rates, calculated branching ratios, and quantum-efficiency relations used in this work are:

$$A_J = \beta_J^{exp} A_{tot} \tag{7}$$

$$\beta_J^{calc} = \frac{A_J}{A_{tot}} \tag{8}$$

$$\eta_r = \frac{\tau_{exp}}{\tau_{rad}},\ W_{NR} = \tau_{exp}^{-1} - \tau_{rad}^{-1} \tag{9}$$

Table 4
Experimental branching ratios β_J^{exp}, radiative rates, and lifetimes (n = 1.8).

Sample	β_1 ($^7F_1$)	β_2($^7F_3$)	β_3($^7F_3$)	β_4($^7F_4$)	$A_{tot}(s^{-1})$	$A_2(s^{-1})$	$A_4(s^{-1})$
Eu-only	0.325	0.195	0.0046	0.475	262.3	51.3	125.0
+0.01K^+	0.127	0.599	0.015	0.259	671.7	402.5	173.7
+0.01Na^+	0.323	0.204	0.0038	0.469	264.3	53.9	123.8

Table 5
Asymmetry ratio R, average lifetime, and internal efficiency.

Sample	$R = I_{613}/I_{595}$	$\tau_{avg}(ms)$	$\eta_r(\%)$
Eu-only	0.656	1.314	34.5
+0.01K^+	5.15	0.593	39.8
+0.01Na^+	0.691	0.519	13.7

Although the absence of the $^5D_0 \rightarrow {}^7F_6$ band prevents reliable assessment of Ω_6, the relative ratio of Ω_2 and Ω_4, can still be evaluated. The calculated parameter ratio Ω_2/Ω_4 was obtained from the relative transition rates as

$$\frac{\Omega_2}{\Omega_4} = 0.472 \times \frac{A_2}{A_4} \tag{10}$$

with the results summarized in Table 6.

The Eu-only and Na^+-doped samples show Ω_4-dominated behavior ($\Omega_2/\Omega_4 \approx 0.2$), typical of a rigid borate lattice stabilizing the $^7F_4$ manifold. In contrast, K^+ incorporation raises the Ω_2/Ω_4 ratio above unity, confirming a strong enhancement of the rank-2 crystal-field component. This trend is consistent with earlier observations in Eu^{3+}-activated glasses, where Ω_4 commonly dominates due to the rigid host structure [51,53]. The enhancement of Ω_2 upon K^+ addition parallels recent observations in alkali-modified silicate and borate glasses, where the incorporation of larger monovalent cations enhances local site asymmetry around Eu^{3+} and promotes hypersensitive transitions, as supported by structural analyses of modifier-ion effects [16,53–56] and Judd–Ofelt trends in alkali-rich borate systems [57]. Furthermore, the observed reduction in η_r for Na^+-co-doped samples follows the behavior reported for other Eu^{3+}-activated borates, in which enhanced phonon-assisted relaxation channels suppress radiative efficiency [52].

In summary, the J–O analysis demonstrates that K^+ incorporation drives Eu^{3+} ions into more asymmetric local environments, thereby intensifying hypersensitive electric-dipole transitions and enhancing radiative efficiency, while Na^+ maintains an Ω_4-governed environment associated with reduced efficiency but greater structural rigidity. These results establish a clear link between alkali co-doping, site symmetry, and photoluminescence dynamics in LiCBO:Eu^{3+} phosphors.

3.6.5. Thermal quenching and activation energy analysis

The thermal quenching behavior of the Eu^{3+} emission in LiCBO-based phosphors was first investigated through temperature-dependent photoluminescence (PL) measurements, as shown in Fig. 10. For the LiCBO:0.05Eu^{3+} sample (Fig. 10a), the emission intensity at 613 nm decreases sharply with increasing temperature up to 390 K, followed by a partial recovery at higher temperatures, which may be attributed to thermally assisted carrier re-trapping or energy transfer processes. A closer examination of the temperature-dependent PL behavior reveals that the anomalous increase in emission intensity above 430 K likely originates from the thermally activated release of charge carriers from shallow defect levels within the LiCBO lattice. These carriers, once liberated, can recombine radiatively at Eu^{3+} centers, leading to partial intensity recovery at elevated temperatures. Such behavior is commonly observed in rare-earth–doped borates and phosphates, where defect-related traps serve as temporary energy reservoirs. At moderate temperatures (300–390 K), non-radiative phonon-assisted transitions dominate, causing emission quenching, while at higher temperatures, defect-mediated carrier reactivation competes with non-radiative losses. This interplay between non-radiative losses and defect-mediated reactivation results in the observed intensity enhancement beyond 430 K. In contrast, the LiCBO:0.05Eu^{3+}:0.01K^+ phosphor (Fig. 10b) exhibits a more monotonic decrease in emission intensity with temperature, indicating a typical thermal quenching behavior without significant re-trapping effects. Meanwhile, the Na^+ co-doped sample (LiCBO:0.05Eu^{3+}:0.01Na^+, Fig. 10c) shows a pronounced quenching trend similar to the K^+-doped sample, although the quenching rate is stronger compared to the pristine composition.

The inset plots in Fig. 10 highlight the temperature evolution of the integrated PL intensity at 613 nm, which clearly illustrates the differences in quenching behavior among the three compositions. Specifically, the undoped Eu^{3+} sample preserves ~54 % of its initial room-temperature intensity at the highest measured temperature, whereas the K^+ and Na^+ co-doped samples maintain ~71 % and ~75 %, respectively. This indicates that alkali co-doping helps to retain higher relative emission intensity at elevated temperatures, although the underlying mechanism may involve defect-related charge compensation and lattice relaxation rather than increased structural rigidity. To quantify this effect, the activation energies (E_a) for thermal quenching were further extracted using Arrhenius-type analysis, as discussed below.

To quantify the thermal quenching behavior, the temperature-dependent intensity data were fitted using the Arrhenius equation:

$$I(T) = \frac{I_o}{1 + Cexp\left(-\frac{E_a}{kT}\right)} \tag{8}$$

where $I(T)$ is the luminescence intensity at temperature T, I_0 is the initial intensity, C is a constant, k is the Boltzmann constant, and E_a is the activation energy. The corresponding Arrhenius plots of $ln[(I_o/I) - 1]$ versus $1/kT$ is fitted by a straight line as shown in Fig. 11. The extracted activation energies were found to be approximately 0.36 eV for LiCBO:0.05Eu^{3+}, 0.15 eV for LiCBO:0.05Eu^{3+},0.01K^+, and 0.16 eV for LiCBO:0.05Eu^{3+},0.01Na^+.These values are in good agreement with previously reported activation energies for Eu^{3+}-activated borate phosphors (0.12–0.35 eV) [13,58,59] and confirm that alkali ion co-doping effectively modifies the local crystal field environment and suppresses non-radiative losses. Notably, the co-doped samples exhibited lower activation energies compared to the undoped Eu^{3+} phosphor. The E_a values for the co-doped samples were found to be lower than that of the undoped Eu^{3+} phosphor. This reduction in activation energy can be explained by the structural and electronic modifications introduced through alkali co-doping. The incorporation of Li^+ or K^+ ions generates charge-compensating defects and local lattice distortions that enhance the energy transfer to Eu^{3+} ions, resulting in higher emission intensity at room temperature. However, these same defects also act as nonradiative channels that become thermally activated at elevated temperatures, increasing phonon coupling and reducing the energy barrier for thermal

Table 6
Judd–Ofelt intensity ratio Ω_2/Ω_4

Sample	A_2/A_4	Ω_2/Ω_4
Eu-only	0.410	0.194
+0.01K^+	2.317	1.09
+0.01Na^+	0.435	0.205

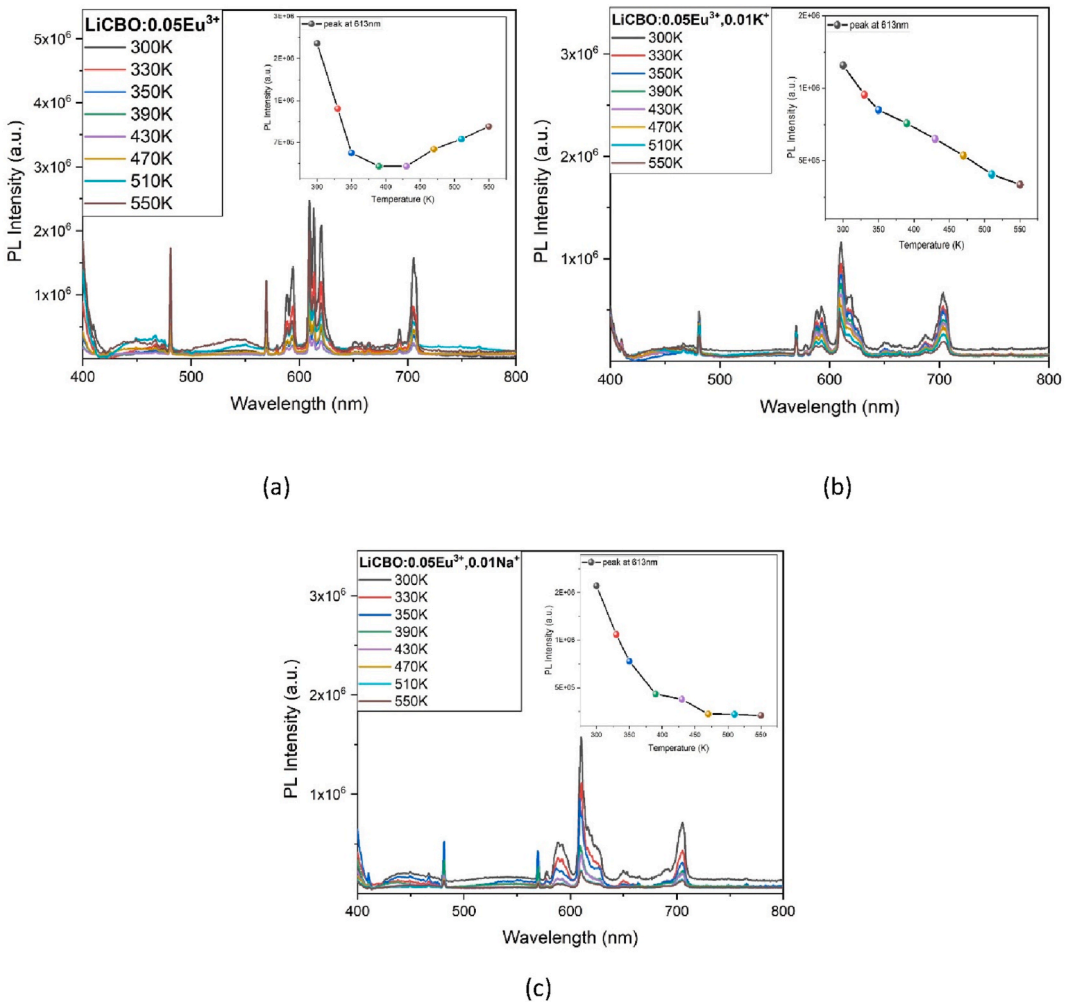

Fig. 10. Temperature-dependent PL spectra of Eu^{3+}-doped LiCBO with (a) no co-doping, (b) K^+ co-doping, and (c) Na^+ co-doping. Insets: temperature dependence of the 613 nm peak intensity.

quenching. Consequently, the co-doped phosphors exhibit lower E_a values, indicating slightly decreased thermal stability despite enhanced room-temperature luminescence. Although the Na^+- and K^+-co-doped samples exhibit lower activation energies (~0.15–0.16 eV) compared to the Eu-only composition (~0.36 eV), they retain a higher fraction of their luminescence intensity at elevated temperatures. This apparent contradiction can be rationalized by considering that alkali incorporation introduces charge-compensated local distortions, which facilitate alternative radiative pathways and reduce the probability of permanent non-radiative trapping. Thus, even though non-radiative channels are thermally accessible at lower energies, the structural relaxation induced by alkali ions helps maintain efficient radiative recombination, leading to better emission stability. It is worth noting that the undoped Eu^{3+} sample exhibits a relatively higher activation energy (~0.36 eV) compared to the Na^+- and K^+-co-doped counterparts (~0.16–0.17 eV). This difference originates from variations in the local Eu^{3+} environment. In the Eu-only composition, the Eu^{3+} ions are accommodated in a structurally more rigid and charge-balanced lattice, requiring higher thermal energy to activate non-radiative channels. By contrast, alkali incorporation introduces local distortions and charge-compensation defects, which act as additional quenching centers and lower the effective energy barrier for thermal depopulation. Furthermore, alkali-assisted structural relaxation facilitates Eu^{3+}–Eu^{3+} energy transfer pathways that are more easily thermally activated, thereby reducing the apparent activation energy.

3.6.6. *Chromaticity coordinates and color emission properties*

The chromaticity coordinates of LiCBO:xEu^{3+}, LiCBO:0.05Eu^{3+},yK^+, and LiCBO:0.05Eu^{3+},yNa^+ phosphors were calculated from the emission spectra and are shown in Fig. 12. For the Eu^{3+}-doped series (Fig. 12a), the CIE coordinates gradually shift toward the red region with increasing Eu^{3+} content, moving from (0.4423, 0.2798) at x = 0.005 to (0.6026, 0.3548) at x = 0.05. This trend reflects the strengthening of the characteristic $^5D_0 \rightarrow {}^7F_2$ transition of Eu^{3+} ions, confirming their efficient incorporation into the host lattice.

For the K^+ co-doped series (Fig. 12b), the chromaticity coordinates are displaced toward the orange-red region compared with the undoped counterpart. With increasing K^+ concentration, a systematic shift of emission color is observed, reaching values around (0.4190, 0.2661) for y = 0.07. This indicates that K^+ incorporation alters the local crystal field around Eu^{3+}, slightly modifying the relative intensity ratio of the red to orange transitions.

Similarly, Na^+ co-doping (Fig. 12c) results in a noticeable adjustment of the emission coordinates. At low Na^+ levels, the phosphors exhibit strong red emission with coordinates close to (0.6026, 0.3548), whereas higher doping concentrations shift the color points toward lower x and y values, e.g., (0.4384, 0.2745) for y = 0.07. This behavior suggests that Na^+ incorporation induces subtle lattice distortions that modify the symmetry of Eu^{3+} sites, thereby influencing the color purity.

To further assess the emission characteristics, the correlated color temperature (CCT) values were calculated using McCamy's empirical relation McCamy [60]:

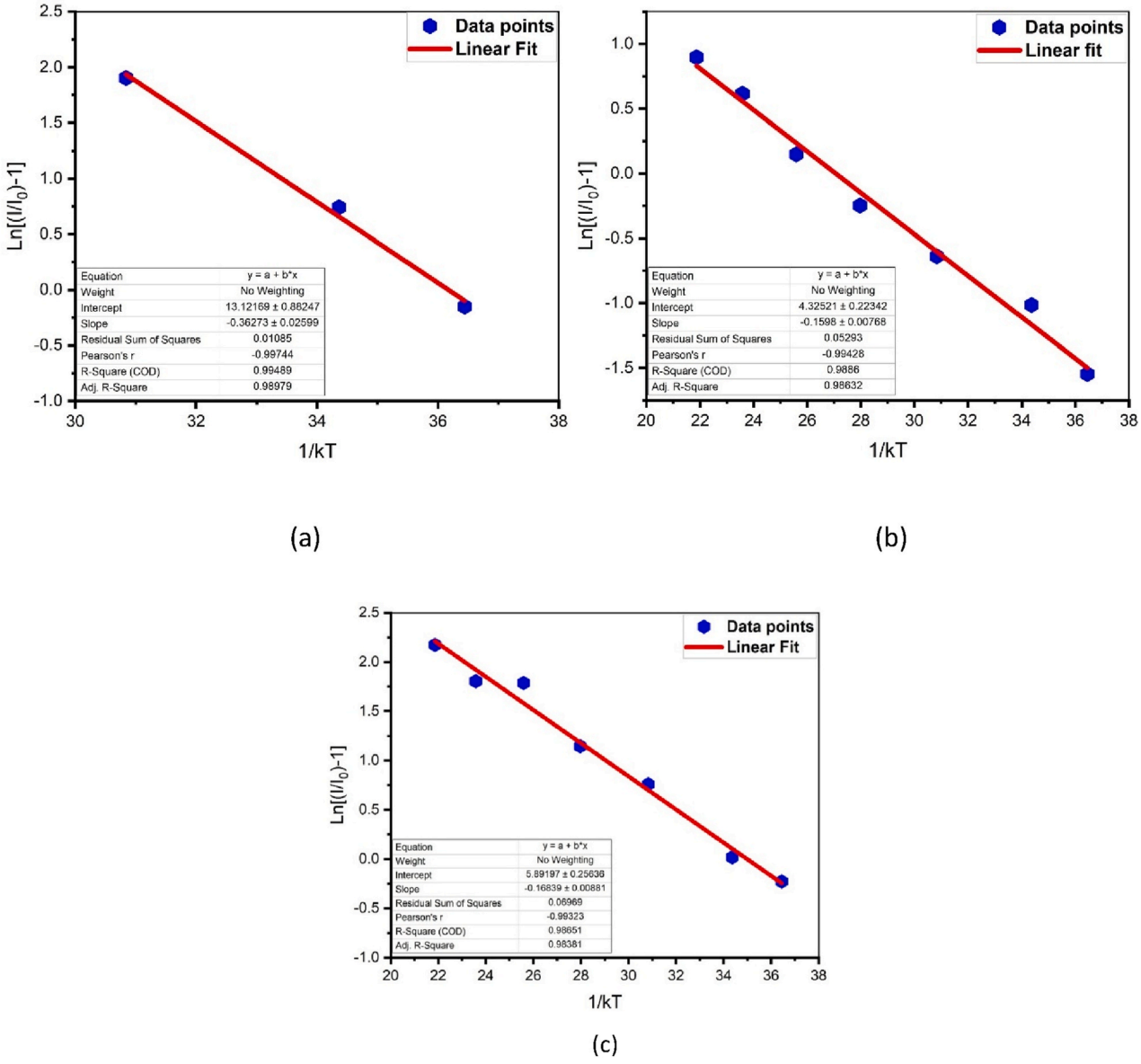

Fig. 11. Temperature-dependent luminescence quenching analysis of LiCBO:0.05Eu^{3+} and alkali ion co-doped samples. Arrhenius plot for (a) LiCBO:0.05Eu^{3+}, (b) LiCBO:0.05Eu^{3+},0.01K^{+}, and (c) LiCBO:0.05Eu^{3+},0.01Na^{+}. Solid red lines represent linear fitting of the experimental data used to estimate activation energies. (For interpretation of the references to color in this figure legend, the reader is referred to the Web version of this article.)

$$n = \frac{x - 0.3320}{y - 0.1858}, CCT\ (K) = -449n^3 + 3525n^2 - 6823.3n + 5520.33 \quad (7)$$

The obtained CCT values are consistently below 2000 K for all samples, placing the emissions in the deep-red to warm-red region. Pure Eu^{3+}-doped samples show values around 1785 K at x = 0.05, while K^{+} and Na^{+} co-doped samples exhibit slightly tuned values ranging between ~1630 and 1950 K depending on dopant concentration. These results confirm that alkali ion co-doping not only adjusts the chromaticity but also preserves the desirable low-CCT red emission, highlighting their applicability in WLEDs and display technologies.

4. Conclusion

In this work, Eu^{3+}-doped LiCBO phosphors were systematically investigated with Na^{+} and K^{+} co-doping to elucidate the correlation between structural modulation and luminescence behavior:

- All samples crystallized in a single-phase orthorhombic structure, where alkali incorporation induced slight lattice distortions and increased microstrain.
- Photoluminescence measurements confirmed the characteristic red emissions of Eu^{3+}, where Na^{+} co-doping strengthened the $^5D_0 \rightarrow {}^7F_4$ transition, broadening the red spectral output.
- The most remarkable effect was observed for K^{+} incorporation, which increased the Ω_2/Ω_4 ratio to values above unity. This clearly indicates enhanced local asymmetry around Eu^{3+} sites and a pronounced activation of the hypersensitive $^5D_0 \rightarrow {}^7F_2$ transition, thereby producing red emission with higher color purity.
- Lifetime and quantum efficiency analyses further showed that K^{+} co-doping improved radiative efficiency, while Na^{+} preserved structural rigidity with moderate trade-offs in emission intensity.
- Thermal quenching studies confirmed that alkali co-doping improved high-temperature emission retention, enhancing the operational stability of the phosphors.

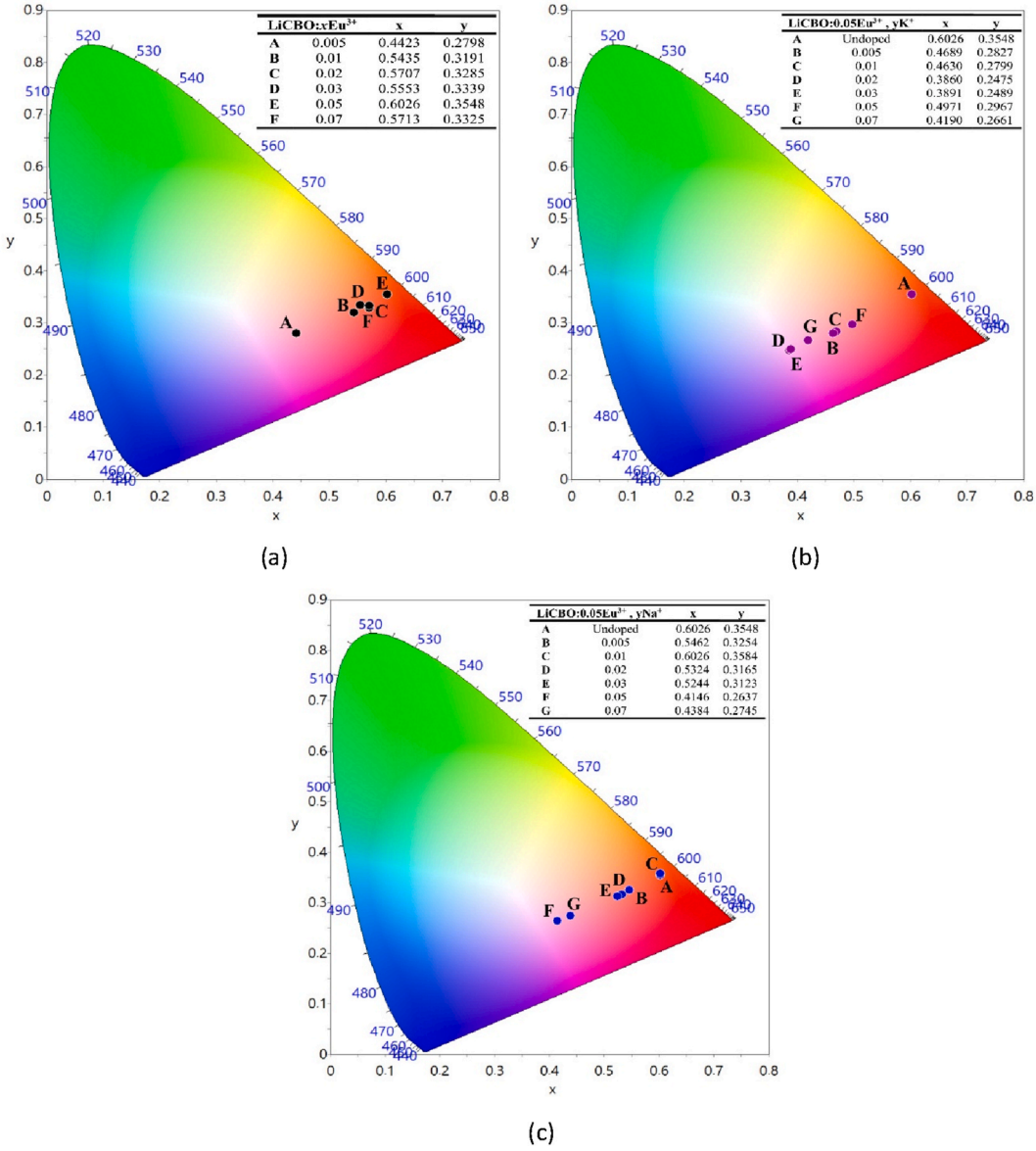

Fig. 12. CIE 1931 chromaticity coordinates of LiCBO:Eu^{3+} phosphors at various dopant concentrations: (a) Eu^{3+} singly doped, (b) Eu^{3+}/K^{+} co-doped, and (c) Eu^{3+}/Na^{+} co-doped samples.

In summary, Na^{+} primarily stabilizes the crystal framework, whereas K^{+} effectively enhances site asymmetry and activates hypersensitive transitions. This dual-alkali strategy provides a powerful pathway for designing next-generation Eu^{3+}-based borate phosphors with superior red emission efficiency and stability.

CRediT authorship contribution statement

Jabir Hakami: Software, Methodology, Investigation, Conceptualization. **M.B. Coban:** Software, Methodology, Investigation. **H. Aydin:** Software, Methodology, Investigation. **U.H. Kaynar:** Software, Methodology, Investigation. **M. Sharahili:** Methodology, Investigation. **O. Madkhali:** Methodology, Investigation. **D. Somaily:** Methodology, Investigation. **N. Can:** Writing – review & editing, Writing – original draft, Supervision, Methodology, Investigation, Formal analysis.

Declaration of competing interest

The authors declare that they have no known competing financial interests or personal relationships that could have appeared to influence the work reported in this paper.

Acknowledgements

The authors gratefully acknowledge the funding of the Deanship of Graduate Studies and Scientific Research, Jazan University, Saudi Arabia, through Project number: (JU- 20250218 -DGSSR- RP -2025).

Data availability

Data will be made available on request.

References

[1] Z. Wang, Z. Yang, P. Li, Q. Guo, Y. Yang, Luminescence characteristics of $LiCaBO_3$:Tb^{3+} phosphor for white LEDs, J. Rare Earths 28 (2010) 30–33, https://doi.org/10.1016/S1002-0721(09)60044-2.

[2] P. Li, Z. Yang, Z. Wang, Q. Guo, Luminescent characteristics of $LiCaBO_3$:Eu^{3+} phosphor for white light emitting diode, J. Rare Earths 27 (2009) 390–393, https://doi.org/10.1016/S1002-0721(08)60257-4.

[3] P. Li, Z. Wang, Z. Yang, Q. Guo, X. Li, Luminescent characteristics of $LiCaBo_3$:M (M=Eu^{3+}, Sm^{3+}, Tb^{3+}, Ce^{3+}, Dy^{3+}) phosphor for white LED, J. Lumin. 130 (2010) 222–225, https://doi.org/10.1016/j.jlumin.2009.08.010.

[4] D.A.E. Somaily, A.S. Altowyan, U.H. Kaynar, H. Aydin, J. Hakami, M.B. Coban, T. Zelai, N. Can, Tunable luminescence and structural modifications in Eu^{3+}/Li^{+} Co-doped $YBa_3(BO_3)_3$ phosphors for LEDs, Mater. Res. Bull. 189 (2025) 113453, https://doi.org/10.1016/j.materresbull.2025.113453.

[5] T. Zheng, M. Runowski, P. Woźny, S. Lis, Influence of matrix on the luminescence properties of Eu^{2+}/Eu^{3+} doped strontium borates: SrB_4O_7, SrB_2O_4 and $Sr_3(BO_3)_2$, exhibiting multicolor tunable emission, J. Alloys Compd. 822 (2020) 153511, https://doi.org/10.1016/j.jallcom.2019.153511.

[6] B. Padlyak, I. Kindrat, V. Protsiuk, A. Drzewiecki, Optical spectroscopy of $Li_2B_4O_7$, CaB_4O_7 and $LiCaBO_3$ borate glasses doped with europium, Ukr. J. Phys. Opt. 15 (2014) 103, https://doi.org/10.3116/16091833/15/3/103/2014.

[7] N.S. Bajaj, S.K. Omanwar, Combustion synthesis and luminescence characteristic of rare earth activated $LiCaBO_3$, J. Rare Earths 30 (2012) 1005–1008, https://doi.org/10.1016/S1002-0721(12)60169-0.

[8] M. Sharma, H. Sharma, I. Charak, H.C. Swart, V. Kumar, Optimization and luminescence studies of Sm^{3+} doped $LiCaBO_3$ phosphors for high-performance white light-emitting diodes, Chem. Phys. Impact 9 (2024) 100696, https://doi.org/10.1016/j.chphi.2024.100696.

[9] A.B. Gawande, R.P. Sonekar, S.K. Omanwar, Synthesis and enhancement of luminescence intensity by co-doping of M^{+} (M=Li, Na, K) in Ce^{3+} doped strontium haloborate, Opt. Mater. (Amst). 36 (2014) 1143–1145, https://doi.org/10.1016/j.optmat.2014.02.017.

[10] A.A. Alsam, U.H. Kaynar, H. Aydin, M.B. Coban, A. Canimoglu, N. Can, Enhanced luminescence and quenching mechanisms in Na^{+} Co-doped $K_7CaY_2(B_5O_{10})_3$:Tb^{3+} phosphors under UV radiation, Appl. Radiat. Isot. 217 (2025) 111635, https://doi.org/10.1016/j.apradiso.2024.111635.

[11] Y.R. Parauha, R.L. Kohale, M. Joshi, H.C. Swart, S.J. Dhoble, Review on advancements in white light phosphor matrices for energy-efficient lighting, Mater. Sci. Semicond. Process. 184 (2024) 108725, https://doi.org/10.1016/j.mssp.2024.108725.

[12] P.N. Parale, A.R. Kadam, S.J. Dhoble, K.V. Dabre, Tailored efficient energy transfer Tb^{3+}, Eu^{3+} activated/co-activated $LiAl(PO_3)_4$ phosphor by substitution of alkali metals: the effect of charge compensation, RSC Adv. 13 (2023) 26179–26188, https://doi.org/10.1039/D3RA03115B.

[13] U.H. Kaynar, H. Aydin, A.S. Altowyan, J. Hakami, M.B. Coban, M. Ayvacikli, E. Ekdal Karali, A. Canimoglu, N. Can, Enhancement of luminescence and thermal stability in Eu^{3+}-doped $K_3Y(BO_2)_6$ with Li^{+} and Na^{+} co-doping, Adv. Powder Technol. 35 (2024) 104695, https://doi.org/10.1016/j.apt.2024.104695.

[14] P. Dang, G. Li, X. Yun, Q. Zhang, D. Liu, H. Lian, M. Shang, J. Lin, Thermally stable and highly efficient red-emitting Eu^{3+}-doped $Cs_3GdGe_3O_9$ phosphors for WLEDs: non-concentration quenching and negative thermal expansion, Light Sci. Appl. 10 (2021) 29, https://doi.org/10.1038/s41377-021-00469-x.

[15] R.D. Shannon, Revised effective ionic radii and systematic studies of interatomic distances in halides and chalcogenides, Acta Crystallogr., Sect. A 32 (1976) 751–767, https://doi.org/10.1107/S0567739476001551.

[16] P. Gao, Q. Liu, J. Wu, J. Jing, W. Zhang, J. Zhang, T. Jiang, J. Wang, Y. Qi, Z. Li, Enhanced fluorescence characteristics of $SrAl_2O_4$:Eu^{2+}, Dy^{3+} phosphor by Co-Doping Gd^{3+} and anti-counterfeiting application, Nanomaterials 13 (2023) 2034, https://doi.org/10.3390/nano13142034.

[17] G. Williamson, W. Hall, X-ray line broadening from filed aluminium and wolfram, Acta Metall. 1 (1953) 22–31, https://doi.org/10.1016/0001-6160(53)90006-6.

[18] J.I. Langford, A.J.C. Wilson, Scherrer after sixty years: a survey and some new results in the determination of crystallite size, J. Appl. Crystallogr. 11 (1978) 102–113, https://doi.org/10.1107/S0021889878012844.

[19] K. Patel, A. Patel, V.P. Jethwa, H. Patel, G.K. Solanki, X-ray diffraction analysis of orthorhombic SnSe nanoparticles by Williamson–Hall, halder–wagner and size–strain plot methods, Chem. Phys. Impact 8 (2024) 100547, https://doi.org/10.1016/j.chphi.2024.100547.

[20] A. Monshi, M.R. Foroughi, M.R. Monshi, Modified scherrer equation to estimate more accurately nano-crystallite size using XRD, World J. Nano Sci. Eng. 2 (2012) 154–160, https://doi.org/10.4236/wjnse.2012.23020.

[21] F.I.H. Rhouma, F. Belkhiria, E. Bouzaiene, M. Daoudi, K. Taibi, J. Dhahri, R. Chtourou, The structure and photoluminescence of a ZnO phosphor synthesized by the sol gel method under praseodymium doping, RSC Adv. 9 (2019) 5206–5217, https://doi.org/10.1039/C8RA09939A.

[22] T. Choudhury, E. Kumi-Barimah, P. Parameswaran Nampi, G.M. Kale, G. Jose, Influence of lattice strain on Er^{3+} ions activated magnesium zirconium phosphate phosphors: morphological, structural, and photoluminescence properties, Mater. Sci. Eng. B 277 (2022) 115582, https://doi.org/10.1016/j.mseb.2021.115582.

[23] A. Rulmont, M. Almou, Vibrational spectra of metaborates with infinite chain structure: $LiBO_2$, CaB_2O_4, SrB_2O_4, Spectrochim. Acta Part A Mol. Spectrosc. 45 (1989) 603–610, https://doi.org/10.1016/0584-8539(89)80013-3.

[24] H.A. Othman, H.S. Elkholy, I.Z. Hager, FTIR of binary lead borate glass: structural investigation, J. Mol. Struct. 1106 (2016) 286–290, https://doi.org/10.1016/j.molstruc.2015.10.076.

[25] M. Priya, M. Dhavamurthy, A.A. Suresh, M.M. Mohapatra, Luminescence and spectroscopic studies on Eu^{3+}-doped borate and boro-phosphate glasses for solid state optical devices, Opt. Mater. 142 (2023) 114007, https://doi.org/10.1016/j.optmat.2023.114007.

[26] A.S. Altowyan, U.H. Kaynar, C. Gök, H. Aydin, J. Hakami, M.B. Coban, A. Canimoglu, N. Can, Photoluminescence characteristics and Judd–Ofelt analysis of $YBa_3(BO_3)_3$:Tb^{3+} phosphors co-doped with Li^{+}, Na^{+}, and K^{+}, J. Lumin. 286 (2025) 121380 https://doi.org/10.1016/j.jlumin.2025.121380.

[27] L. Song, Y. Wang, A.C. Hannon, S. Feller, W. Li, Y. Zhou, F. Zhu, Structural investigation of lithium borate glasses by Raman spectroscopy: quantitative evaluation of structural units and its correlation with density, J. Non-Cryst. Solids 616 (2023) 122478, https://doi.org/10.1016/j.jnoncrysol.2023.122478.

[28] N.S. Ezra, I.S. Mustafa, M.I. Sayyed, K.K. Dakok, T.H. Khazaalah, G.I. Efenji, M. Jamil, H.S. Naeem, A.O. Oke, I.M. Fadhirul, A.S.A. Idriss, Synthesis and effect of $MgSO_4$ co-doping on the optical, IR, and raman spectroscopic studies of Eu^{3+}-Doped alkaline Silica borate glasses produced with SLS glass as a silica source, Silicon 16 (2024) 6085–6097, https://doi.org/10.1007/s12633-024-03134-1.

[29] H. Guo, T. Wang, B. Liu, W. Gao, L. Xiu, Z. Cui, H. Zhang, Q. Ma, S. Wang, Z. Li, L. Guo, G. Yan, S. Yu, X. Yu, X. Xu, J. Qiu, Fabrication and photoluminescence characteristics of novel red-emitting Ba_2LuNbO_6:Eu^{3+} double-perovskite phosphors on near UV WLEDs, J. Rare Earths 40 (2022) 1173–1180, https://doi.org/10.1016/j.jre.2021.06.006.

[30] R.S. Yadav A. Bahadur Monika, S.B. Rai, Multicolor tunable bright photoluminescence in Ca^{2+}/Mg^{2+} modified Eu^{3+} doped $ZnGa_2O_4$ phosphors under UV excitation for solid state lighting applications, RSC Adv. 13 (2023) 20164–20178, https://doi.org/10.1039/D3RA03215A.

[31] W. Zhang, Y. Chen, X. Geng, Y. Yang, L. Xiao, Synthesis and luminescence properties of $LiBaB_9O_{15}$:Eu^{3+} single-component red-light emitting phosphors, J. Lumin. 224 (2020) 117324, https://doi.org/10.1016/j.jlumin.2020.117324.

[32] A.P. Shablinskii, A.V. Povolotskiy, A.A. Yuriev, Y.P. Biryukov, R.S. Bubnova, M. S. Avdontceva, S.Y. Janson, S.K. Filatov, Novel red-emitting $BaBi_2B_4O_{10}$:Eu^{3+} phosphors: synthesis, crystal structure and luminescence, Symmetry (Basel). 15 (2023) 918, https://doi.org/10.3390/sym15040918.

[33] N. Yang, J. Li, Z. Zhang, D. Wen, Q. Liang, J. Zhou, J. Yan, J. Shi, Delayed concentration quenching of luminescence caused by Eu^{3+} -Induced phase transition in $LaSc_3(BO_3)_4$, Chem. Mater. 32 (2020) 6958–6967, https://doi.org/10.1021/acs.chemmater.0c02203.

[34] G. Blasse, Energy transfer in oxidic phosphors, Phys. Lett. A 28 (1968) 444–445, https://doi.org/10.1016/0375-9601(68)90486-6.

[35] D.L. Dexter, A theory of sensitized luminescence in solids, J. Chem. Phys. 21 (1953) 836–850, https://doi.org/10.1063/1.1699044.

[36] U.H. Kaynar, M.B. Coban, J. Hakami, A.S. Altowyan, H. Aydin, M. Ayvacikli, N. Can, Enhanced luminescence of Eu^{3+} in $LaAl_2B_4O_{10}$ via energy transfer from Dy^{3+} doping, Spectrochim. Acta Part A Mol. Biomol. Spectrosc. 321 (2024) 124711, https://doi.org/10.1016/j.saa.2024.124711.

[37] K.K. Mahato, S.B. Rai, A. Rai, Optical studies of Eu^{3+} doped oxyfluoroborate glass, Spectrochim. Acta Part A Mol. Biomol. Spectrosc. 60 (2004) 979–985, https://doi.org/10.1016/S1386-1425(03)00328-7.

[38] G. Annadurai, B. Devakumar, H. Guo, B. Li, L. Sun, X. Huang, Photoluminescence properties of novel $Ba_2Lu_5B_5O_{17}$:Eu^{3+} red emitting phosphors with high color purity for near-UV excited white light emitting diodes, RSC Adv. 8 (2018) 30396–30403, https://doi.org/10.1039/C8RA06457A.

[39] O. Madkhali, Ü.H. Kaynar, Y. Alajlani, M.B. Coban, J.G. Guinea, M. Ayvacikli, J. F. Pierson, N. Can, Structural and temperature dependence luminescence characteristics of RE (RE=Eu^{3+}, Dy^{3+}, Sm^{3+} and Tb^{3+}) in the new gadolinium aluminate borate phosphor, Ceram. Int. 49 (2023) 19982–19995, https://doi.org/10.1016/j.ceramint.2023.03.120.

[40] J. Deng, Z. Wang, W. Zhou, J. Min, M. Yu, X. Jiang, H. Ding, Z. Xue, M. Jin, F. Gao, Z. Cheng, G. Luo, Enhancement of luminescence properties of $Ca_2Al_2SiO_7$:Eu^{3+} red phosphors by Li^{+}, Na^{+}, K^{+}, Mg^{2+} charge compensators, Ceram. Int. 49 (2023) 39568–39575, https://doi.org/10.1016/j.ceramint.2023.09.308.

[41] V. Jubera, J. Chaminade, A. Garcia, F. Guillen, C. Fouassier, Luminescent properties of Eu3+-activated lithium rare earth borates and oxyborates, J. Lumin. 101 (2003) 1–10, https://doi.org/10.1016/S0022-2313(02)00335-6.

[42] A.S. Altowyan, M.B. Coban, U.H. Kaynar, E.A. Çin, M. Ayvacikli, J. Hakami, N. Can, Structural and photoluminescent analysis of novel Eu^{3+} and Dy^{3+} Co-doped ZnO nanoparticles by incorporation of Li^{+} and K^{+} ions, Ceram. Int. 50 (2024) 14529–14541, https://doi.org/10.1016/j.ceramint.2024.01.366.

[43] M.V. dos S. Rezende, M.E.G. Valério, R. Mouta, E.M. Diniz, C.W. de A. Paschoal, Mechanism of luminescent enhancement in Ba_2GdNbO_6:Eu^{3+} perovskite by Li^{+} co-doping, J. Phys. Condens. Matter 26 (2014) 505502. http://arxiv.org/abs/1403.0977.

[44] C.M. Nandanwar, A.N. Yerpude, N.S. Kokode, S.J. Dhoble, Effect of alkali metal ions A^{+} ($A = K^{+}$, Na^{+} and Li^{+}) on the photoluminescence properties of $Sr_3Bi(PO_4)_3$: Sm^{3+} phosphors prepared by wet chemical synthesis, Res. Opt. 12 (2023) 100456, https://doi.org/10.1016/j.rio.2023.100456.

[45] C.M. Nandanwar, N.S. Kokode, A.V. Nande, A.N. Yerpude, R.S. Yadav, S.J. Dhoble, Photoluminescence studies of $Sr_3P_4O_{13}$: Eu3+ phosphor prepared by wet chemical method: structural properties, charge compensation via alkali metal ions and Judd-Ofelt analysis, J. Mol. Struct. 1322 (2025) 140224, https://doi.org/10.1016/j.molstruc.2024.140224.

[46] C.M. Nandanwar, A.N. Yerpude, N.S. Kokode, S.J. Dhoble, Effect of charge compensators A^{+} (A^{+} = Li, Na and K) on photoluminescence properties of $Ba_2Ca(PO_4)_2$:Eu^{3+} phosphor for solid state lighting, J. Mater. Sci. Mater. Electron. 34 (2023) 1464, https://doi.org/10.1007/s10854-023-10889-7.

[47] R. Chatterjee, S. Saha, D. Sen, K. Panigrahi, U.K. Ghorai, G.C. Das, K. K. Chattopadhyay, Neutralizing the charge imbalance problem in Eu^{3+}-Activated $BaAl_2O_4$ nanophosphors: theoretical insights and experimental validation considering K^{+} codoping, ACS Omega 3 (2018) 788–800, https://doi.org/10.1021/acsomega.7b01525.

[48] G.L. Bhagyalekshmi, D.N. Rajendran, Luminescence dynamics of Eu^{3+} activated and co-activated defect spinel zinc titanate nanophosphor for applications in WLEDs, J. Alloys Compd. 850 (2021) 156660, https://doi.org/10.1016/j.jallcom.2020.156660.

[49] B.R. Judd, Optical absorption intensities of rare-earth ions, Phys. Rev. 127 (1962) 750–761, https://doi.org/10.1103/PhysRev.127.750.
[50] G.S. Ofelt, Intensities of Crystal spectra of rare-earth ions, J. Chem. Phys. 37 (1962) 511–520, https://doi.org/10.1063/1.1701366.
[51] W.T. Carnall, P.R. Fields, K. Rajnak, Electronic energy levels of the trivalent lanthanide aquo ions. IV. Eu^{3+}, J. Chem. Phys. 49 (1968) 4450–4455, https://doi.org/10.1063/1.1669896.
[52] R. Shi, A.-V. Mudring, Phonon-mediated nonradiative relaxation in Ln^{3+}-Doped luminescent nanocrystals, ACS Mater. Lett. 4 (2022) 1882–1903, https://doi.org/10.1021/acsmaterialslett.2c00595.
[53] K. Mariselvam, R. Arun Kumar, M. Jagadeesh, Spectroscopic properties and Judd-Ofelt analysis of Eu^{3+} doped barium bismuth fluoroborate glasses, Opt. Mater. 84 (2018) 427–435, https://doi.org/10.1016/j.optmat.2018.07.044.
[54] Y. Nageno, H. Takebe, K. Morinaga, T. Izumitani, Effect of modifier ions on fluorescence and absorption of Eu^{3+} in alkali and alkaline earth silicate glasses, J. Non-Cryst. Solids 169 (1994) 288–294, https://doi.org/10.1016/0022-3093(94)90324-7.
[55] N.T.Q. Lien, N.N. Trac, P. Van Do, H. Van Tuyen, Judd-Ofelt analysis of Eu^{3+} and adjustable emission in Eu^{3+}/Eu^{2+} co-doped sodium aluminosilicate glasses, J. Phys. Chem. Solid. 164 (2022) 110637, https://doi.org/10.1016/j.jpcs.2022.110637.
[56] W.A. Pisarski, Judd–Ofelt analysis and emission properties of Dy^{3+} ions in borogermanate glasses, Materials 15 (2022) 9042, https://doi.org/10.3390/ma15249042.
[57] S. Tanabe, T. Ohyagi, N. Soga, T. Hanada, Compositional dependence of Judd-Ofelt parameters of Er^{3+} ions in alkali-metal borate glasses, Phys. Rev. B 46 (1992) 3305–3310, https://doi.org/10.1103/PhysRevB.46.3305.
[58] S. Cui, X. He, D. Wang, J.-X. Wang, Y. Pu, J.-F. Chen, Tuning the doping of Europium in gadolinium borate microparticles at mesoscale toward efficient production of red phosphors, ACS Omega 4 (2019) 14497–14502, https://doi.org/10.1021/acsomega.9b01656.
[59] Z. Tang, F. Du, H. Liu, Z. Leng, X. Sun, H. Xie, M. Que, Y. Wang, Eu^{2+}-Doped layered double borate phosphor with ultrawide near-infrared spectral distribution in response to ultraviolet–blue light excitation, Adv. Opt. Mater. 10 (2022) 2102204, https://doi.org/10.1002/adom.202102204.
[60] C.S. McCamy, Correlated color temperature as an explicit function of chromaticity coordinates, Color Res. Appl. 17 (1992) 142–144, https://doi.org/10.1002/col.5080170211.